buildings

MDPI

Article

Seismic Fragility Functions for Non-Seismically Designed RC Structures Considering Pounding Effects

Hossameldeen Mohamed [1] and Xavier Romão [2,*]

[1] Faculty of Engineering, Aswan University, Aswan 81542, Egypt; hossam.ahmed@aswu.edu.eg
[2] CONSTRUCT-LESE, Faculty of Engineering, University of Porto, 4200-465 Porto, Portugal
* Correspondence: xnr@fe.up.pt

Abstract: The proposed study develops fragility functions for non-seismically designed reinforced concrete structures considering different pounding configurations. The study addresses an existing research gap, since large-scale seismic risk assessment studies involving the seismic performance assessment of building portfolios usually do not involve fragility functions accounting for the possibility of pounding. The selected structures include configurations involving different separation distance values and exhibiting floor-to-floor pounding, floor-to-column pounding, pounding between structures with a significant height difference, and pounding between structures with a significant mass difference. The behaviour of these pounding configurations was analysed using incremental dynamic analysis and compared with that of the corresponding control cases (i.e., individual structures with no interaction with other structures). The results indicate the type of failure mechanism that contributes to the global collapse of the different configurations and the influence of the separation distance. Results highlight the main differences between the expected performance of different pounding configurations with respect to the occurrence of the failure mechanism that governs their collapse. Finally, results indicate that large-scale seismic risk assessment studies should consider fragility functions accounting for different pounding configurations when the possibility of pounding is not negligible, except in cases involving floor-to-floor pounding.

Keywords: RC frame; pounding; incremental dynamic analysis; fragility; failure mechanism; separation distance

Citation: Mohamed, H.; Romão, X. Seismic Fragility Functions for Non-Seismically Designed RC Structures Considering Pounding Effects. *Buildings* **2021**, *11*, 665. https://doi.org/10.3390/buildings11120665

Academic Editor: Elena Ferretti

Received: 23 November 2021
Accepted: 13 December 2021
Published: 20 December 2021

1. Introduction

Existing research addressing the seismic performance assessment of building portfolios for the purpose of regional-scale seismic risk assessment studies is often based on several simplified assumptions [1,2]. Some of these assumptions are related to the methodological approach underlying the development of the fragility functions that represent the expected seismic performance of the building typologies under consideration for several performance levels. Typically, the development of analytical fragility functions [3] involves a series of simplifications (e.g., simplified structural models and/or simplified methods of analysis) that, nonetheless, do not prevent the analyses from capturing the main features of the seismic performance of the corresponding building typologies [4]. Still, when simulating the seismic performance of buildings, most existing studies that have developed fragility functions of building typologies do not consider that such buildings have the possibility to interact (i.e., collide) with adjacent ones [5–7], although this phenomenon can lead to a higher probability of collapse [8–11].

During earthquakes, buildings vibrate and undergo lateral displacements that may lead to collisions with adjacent buildings if the separation between them is insufficient. These collisions, commonly termed as the pounding effect, lead to a different dynamic response of buildings, as well as to different load paths, than those found when analysing a building with no lateral interaction with adjacent buildings. Since the latter scenario is the one underlying conventional seismic design procedures, the failure modes found in

buildings undergoing pounding are also expected to be different [9,12–15]. This issue has been identified in several post-earthquake surveys [8,13,15] where buildings exhibiting pounding effects were seen to have a higher risk of collapse or developed severe damage levels. Damage observed in adjacent buildings that underwent pounding varied from local damage in infill walls to more severe damage such as shear failure of columns and even collapse. To mitigate the risk associated with the pounding effect, design codes suggest using a seismic separation distance between adjacent buildings defined as a function of their individual elastic response [16–18]. However, existing adjacent buildings are often found to have an inadequate separation distance [14,19,20].

Given the variability of buildings found in urban areas, pounding configurations between buildings can involve several possibilities. For example, pounding configurations can involve buildings with equal heights or different heights, and the contact type between adjacent buildings can be floor-to-floor or floor-to-column. Furthermore, adjacent buildings can be part of the same construction (e.g., different wings of a building separated by structural joints, where the wings are expected to have similar design characteristics), or they can be part of independent constructions (in which case they may have significantly different design characteristics). In addition, it is worth noting that urban planning rules can also influence and facilitate the occurrence of certain pounding configurations, e.g., when urban planning allows adjacent buildings to be constructed with different heights or floor-levels. Post-earthquake surveys have demonstrated that the pounding configuration plays a key role in the performance of buildings that undergo pounding [9,21], and buildings with a particular configuration are more likely to experience severe damage than others. Configurations that have been identified as more vulnerable include adjacent buildings exhibiting floor-to-column alignments [21–24], adjacent buildings with significant mass or height differences [22,25], buildings at the end of a row of buildings [21,26], and buildings likely to experience eccentric pounding [9,13,15,21,27]. Therefore, it can be seen that assessing the seismic risk of building portfolios at the urban or regional level with more realism requires the availability of fragility functions that account for the occurrence of these different pounding phenomena.

Research addressing the structural response of adjacent buildings involving pounding started in the early 1970s [28,29] based on post-earthquake field observations. Over the years, several numerical and experimental studies have been developed to analyse this issue (e.g., see [19,21,30–42] among others) and highlighted that an adequate modelling of the impact between adjacent buildings is fundamental. Among other approaches, the force-based model involving either a linear or nonlinear spring, with or without a viscous damper, was found to be the most adequate approach for computational implementation, given its balance between simplicity and accuracy, particularly for computationally-intense applications [34,43–45]. Among the research studies developed so far, a number of them involved realistic building configurations and were conducted to address the pounding effect on the global structural response during seismic actions (e.g., see [19,32] among others). Overall, several of these studies have found that pounding influences the response of adjacent buildings in terms of displacements [32,37], as well as in terms of acceleration, namely during the impacts [33,38]. Nevertheless, the majority of studies addressing the pounding phenomenon do not consider it from a probabilistic point of view [13,19,21,37,46]. As such, only a few studies have dealt with the development of fragility functions for buildings that undergo pounding [19,47,48]. Although these studies have found that different pounding configurations may have different impacts on the resulting fragility functions, their results are not fully generalised. Therefore, further research addressing a larger number of pounding configurations and building sizes is needed to better understand these effects, particularly for existing buildings constructed without seismic design considerations. Furthermore, such research will also provide important results to understand if fragility functions developed for buildings without considering pounding can also be used for buildings likely to undergo pounding, with negligible errors in the performance assessment of those buildings.

To address some of the referred research needs, a comprehensive study of reinforced concrete (RC) buildings undergoing pounding was performed using probabilistic performance-based analysis in order to derive fragility functions associated with different pounding configurations. The presented research involves several case studies representing a large number of pounding configurations of adjacent non-seismically designed RC frames. These include configurations exhibiting floor-to-floor pounding, floor-to-column pounding, pounding between structures with a significant height difference, and pounding between structures with a significant mass difference. The selected pounding configurations were analysed using incremental dynamic analysis (IDA) [49] for a large group of real ground motion records, and fragility functions associated with several limit states were then derived for the critical structure of each configuration. The results that are obtained were also used to analyse the effect of the pounding configuration on the overall performance of the critical structure of each configuration, particularly regarding the mechanisms that lead to collapse. Moreover, the effect of the separation distance is specifically addressed, given its impact on the global performance of the referred critical structures. Finally, the results of the study provide insights about the possibility of using fragility functions that do not consider the effect of pounding for building typologies that may experience pounding.

2. Methodology

As referred before, the variability of buildings in urban areas leads to the occurrence of different pounding configurations, where some might be more vulnerable than others. In order to analyse the impact of pounding on the seismic performance of RC buildings with different configurations, four building systems with a different number of storeys were selected herein. These systems were first analysed separately to establish control cases and were then used to generate several configurations of adjacent buildings. For the control cases, linear time history analyses were performed, using a set of ground motions compatible with the design response spectrum, to obtain the elastic lateral response and quantify a reference value for the seismic separation distance. The seismic performance of these control cases was then also determined using IDA. Several adjacent building configurations involving pairs of building with different floor alignments were then defined (with and without a separation distance whose value is based on the reference value), and also analysed using IDA. The results obtained provide the basis for discussing the likelihood of a given collapse mechanism as a function of the buildings involved in a pounding configuration. Furthermore, the overall performance of the critical structure of each pounding configuration was analysed and compared with that of the corresponding control case for several limit states. This analysis was performed in probabilistic terms by deriving fragility functions for those limit states and particular attention was given to the influence of the separation distance. To summarise the adopted methodology, Figure 1. illustrates the main steps involved in the proposed analysis.

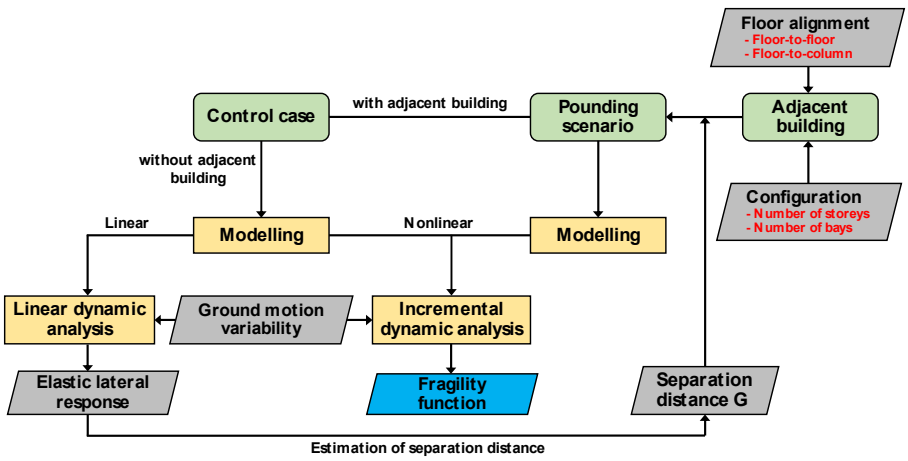

Figure 1. Flowchart describing the adopted methodology.

3. Characterisation of the Selected Building Systems

The analysed building systems are based on four residential RC buildings designed for gravity loads only. The building configurations range from low- to mid-rise buildings regular in plan and over the height that are representative of Egyptian practice. All buildings have a storey height equal to 3.0 m, as well as a concrete strength and a yield strength of the steel reinforcement equal to 25 MPa and 400 MPa, respectively. The plan view of a typical storey of these buildings is presented in Figure 2. Although these buildings are non-seismically designed, they are seen to be representative of older buildings found in the seismic zones of the Egyptian territory, since the current seismic design provisions have only been enforced after the 1992 Cairo earthquake [50]. Furthermore, according to the current Egyptian design code, seismic design is not mandatory for buildings with a height up to 10 m in Zone 1 (which corresponds to a peak ground acceleration (PGA) of 0.1 g) and a height up to 8 m in Zone 2 (which corresponds to a PGA of 0.125 g) [18], and it is not clear if seismic design is commonly considered for other buildings.

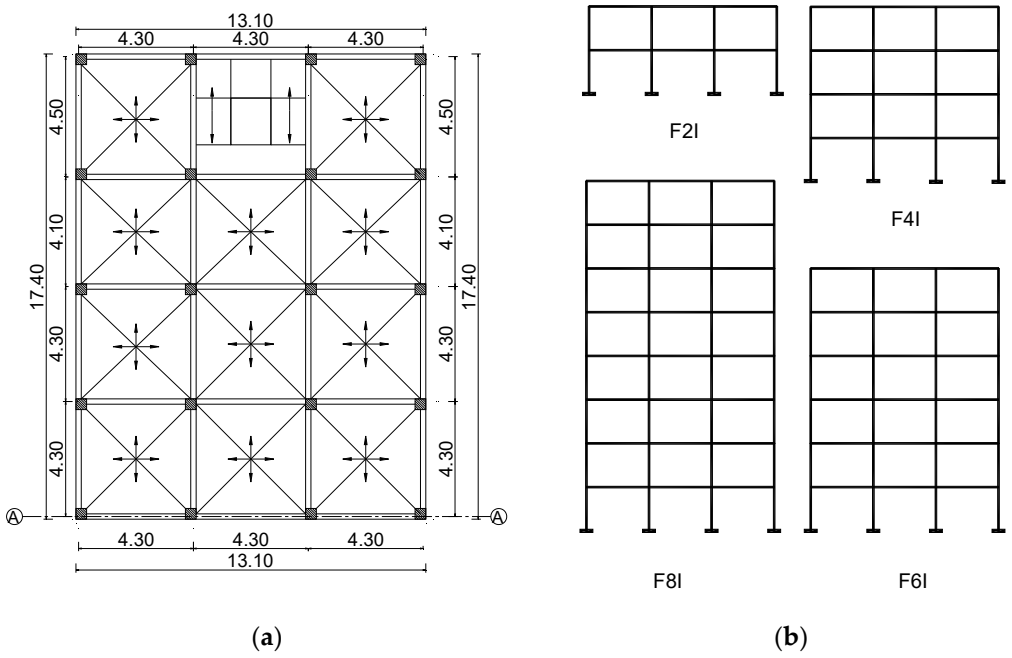

Figure 2. (**a**) Plan view of a typical storey of the considered buildings and (**b**) representation of the considered reference frames (frames of the A-axis in the plan view) (all dimensions are in m).

The selected case study structures are also represented in Figure 2 and correspond to the exterior frame of each building identified as the A-axis (Figure 2a), hereon termed as the reference frame. The designations F2I, F4I, F6I, and F8I are used hereafter to refer to the individual two-, four-, six-, and eight-storey reference frames, respectively (Figure 2b). All the columns of the frames are 30 × 30 cm^2 except the internal columns of F8I, which are 40 × 40 cm^2. The longitudinal reinforcement of all the columns is made of eight evenly distributed ∅12 mm bars, while the transversal reinforcement is made of a two-leg hoop and a crosstie made of ∅6 mm bars and with a spacing of 15 cm. All the beams of the frames have a cross-section of 25 × 40 cm^2. The upper and lower longitudinal reinforcement of all the beams is made of 4 ∅12 mm bars, while the shear reinforcement is made of two-leg 6 mm stirrups with a 15 cm spacing. The fundamental period of the reference frames was found to be 0.39 s, 0.76 s, 1.14 s, and 1.50 s for the F2I, F4I, F6I, and F8I frames, respectively. Different arrangements of these frames were considered to simulate different scenarios of adjacent buildings (i.e., in terms of number of bays and number of storeys). To simulate different scenarios regarding the type of contact between adjacent buildings, two different floor alignments were also considered: buildings with aligned floor levels, leading to a floor-to-floor pounding configuration, and buildings with non-aligned floor levels, leading

to a floor-to-column pounding configuration. Further details about the characteristics of the different frame arrangements and the considered pounding configurations are provided in the next section.

4. Numerical Modelling

4.1. Modelling of the RC Elements

The considered structures were simulated in the OpenSees computer software (version 3.0.3) [51]. Figure 3 provides a visual description of the modelling strategy that was implemented for the RC frame elements. As can be seen, a lumped plasticity approach was adopted to simulate the nonlinear behaviour of all the structural elements using rotational springs at the end of each element [52–57]. A shear failure model was also coupled with the flexural springs of columns given that pounding can lead to excessive shear forces. The beam-column joints were considered as rigid elements. The behaviour of the rotational springs was defined using the trilinear moment-rotation curve proposed in [54], including a monotonic moment-rotation backbone defined as shown in Figure 4a. The properties of the backbone curve of all columns were determined considering an axial force corresponding to the seismic load combination (G + 0.3Q), where G and Q stand for the permanent loads and the quasi-permanent live load, respectively. The yielding moment M_y and the yielding rotation capacity θ_y were determined according to [58] while the remaining parameters (i.e., the capping rotation θ_{cap}, the ultimate rotation θ_u, the capping moment M_c, and the residual moment M_r) were obtained based on the proposal of [54].

The shear failure model adopted herein follows the main principles proposed in [56,59]. As such, a trilinear limit curve was defined to identify the shear force degradation surface. The definition of this surface is based on the proposal by [60] where the authors established the shear failure zone as a limit curve with three branches limited by the maximum shear capacity V_n of the element and by a lower limit of $0.70V_n$, with a transition zone between shear deformation levels that corresponds to flexural ductility levels of 2 to 6, as shown in Figure 4b. The shear capacity V_n is computed based on the expression proposed in ASCE/SEI 41-17 [61]. The initial stiffness K_{ini} and the degraded stiffness $K^t{}_{deg}$ (after shear failure is detected, see Figure 5) are defined based on the expressions proposed in [62] and [57], respectively. Since the flexural and the shear springs at a given member end are modelled in series [60], the degraded stiffness K_{deg} assigned to the shear spring definition is obtained by subtracting the stiffness of the flexural spring K_{flex} from the degraded stiffness $K^t{}_{deg}$. By considering this modelling strategy, all the relevant failure mechanisms can be simulated. As can be seen in Figure 5, the shear spring coupled with the flexural rotational spring can represent the different types of expected failure mechanisms such as flexure failure (in which the member is able to reach a shear capacity V_f governed by the maximum moment in flexure), flexure-shear failure, or shear failure. Furthermore, the adopted modelling strategy can be adapted to account for the different pounding configurations since the elastic element of each member can be divided into multiple segments to introduce extra nodes needed for simulating the different floor alignments without leading to numerical instability.

The hysteretic behaviour of the moment-rotation curves was modelled using the *hysteretic* material of OpenSees as suggested in [63]. Stiffness, strength, and unloading stiffness degradation were considered in the hysteresis curves as illustrated in Figure 6. The unloading stiffness degradation was implemented using the beta factor of the *hysteretic* material. A beta factor of 0.75 was used for the columns and of 0.85 for the beams in order to introduce higher degradation for the latter [64]. The *hysteretic* material parameters related to pinching and to damage due to ductility and dissipated energy were all set equal to zero.

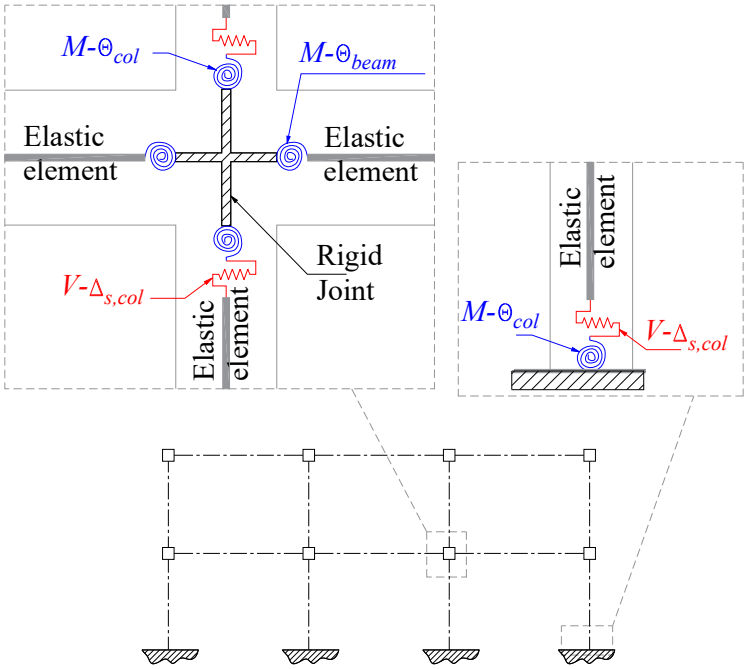

Figure 3. Nonlinear modelling approach adopted for RC elements.

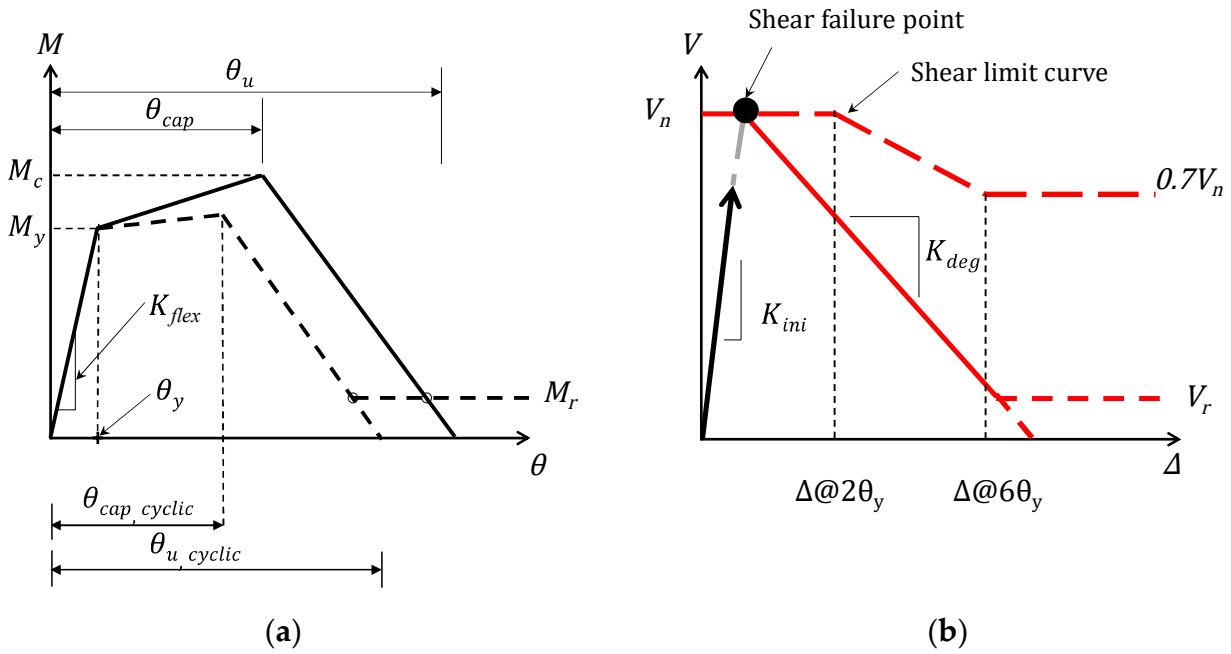

Figure 4. Modelling backbone adopted for the simulation of the pure flexural response spring (no shear spring associated) (**a**) and the pure shear response spring (no rotational spring associated) (**b**).

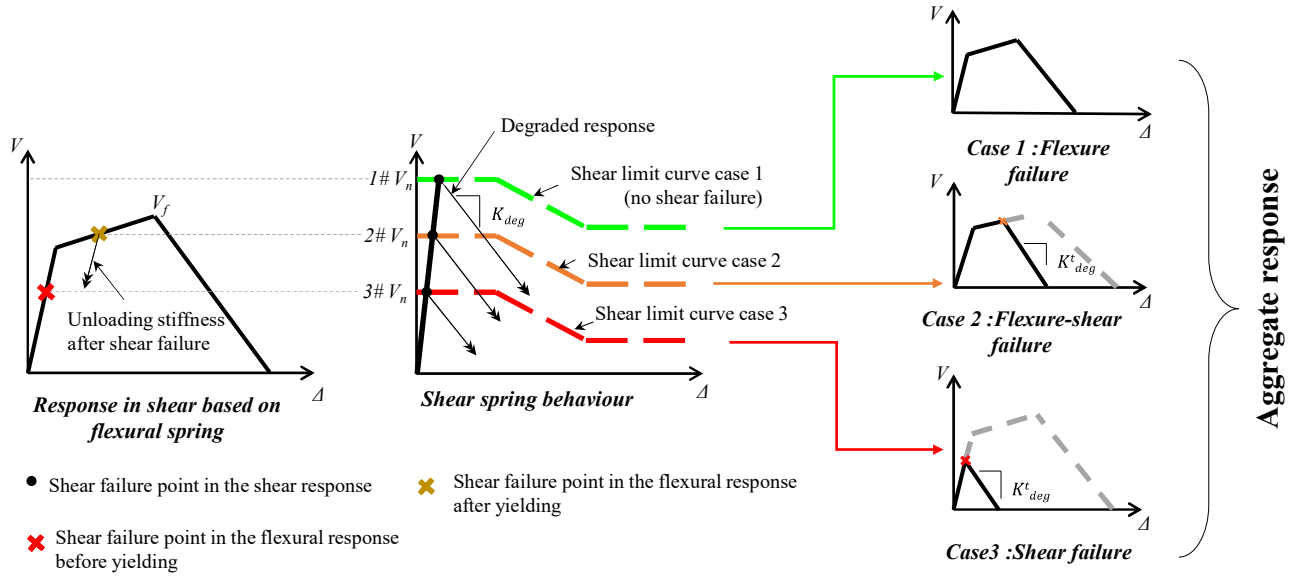

Figure 5. Expected behaviour of columns by coupling the flexural spring with the shear spring.

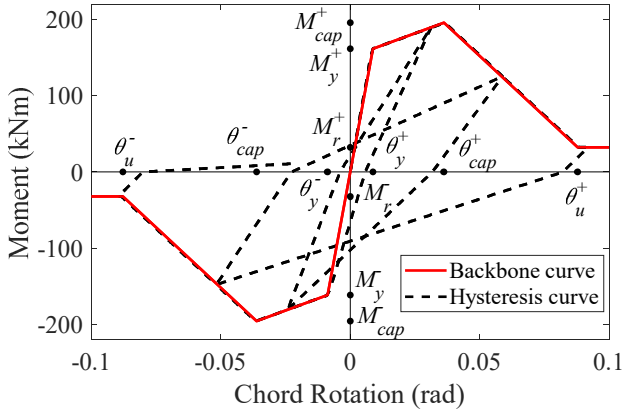

Figure 6. Moment-rotation backbone curve and hysteresis loop simulated by the OpenSees *hysteretic* model.

4.2. Modelling of the Impact Forces

The numerical simulation of the pounding effect in RC buildings involves dealing with two highly nonlinear aspects: the plastic deformations and the contact mechanism. The combination of these two aspects makes finding the analytical solution for the behaviour of pounding systems a highly complex problem. Modelling approaches found in the literature for analysing this type of behaviour can be categorised into two main approaches: the restitution-based stereomechanical approach and the force-based approach. The former is based on laws of energy conservation and momentum [44,65–67], while the latter directly simulates the interaction between colliding structures by introducing an impact force $\overline{F}_p$ during the impact stage [68,69]. Given the limitations of integrating the first approach with multi-degree of freedom systems, and its inability to consider non-simultaneous impacts, as well as the transient forces and deformations that are developed during the impact [44,70], the vast majority of the conducted research has been found to use the force-based approach (e.g., see [19,32,44], among others).

In the force-based approach, the two colliding structural systems x and y are considered as shown in Figure 7. The equation of motion of the two-structure system (x and y) under an earthquake excitation $\ddot{u}_g$ can be expressed as:

$$\begin{bmatrix} m_x & 0 \\ 0 & m_y \end{bmatrix} \begin{Bmatrix} \ddot{u}_x \\ \ddot{u}_y \end{Bmatrix} + \begin{bmatrix} c_x & 0 \\ 0 & c_y \end{bmatrix} \begin{Bmatrix} \dot{u}_x \\ \dot{u}_y \end{Bmatrix} + \begin{bmatrix} k_x & 0 \\ 0 & k_y \end{bmatrix} \begin{Bmatrix} u_x \\ u_y \end{Bmatrix} + \begin{Bmatrix} \overline{F_p} \\ -\overline{F_p} \end{Bmatrix} = -\begin{bmatrix} m_x & 0 \\ 0 & m_y \end{bmatrix} \begin{Bmatrix} \ddot{u}_g \\ \ddot{u}_g \end{Bmatrix} \quad (1)$$

where u_i, $\dot{u}_i$, and $\ddot{u}_i$ are the response in terms of displacement, velocity, and acceleration, respectively, of the ith system (x or y, according to the suffix) along the excitation direction, while m_i, c_i, and k_i are the mass, damping, and stiffness matrices, respectively, of the ith system (x or y, according to the suffix). The vector $\{\overline{F_p}, -\overline{F_p}\}$ contains the pounding forces representing the interaction between the two systems during the collision. Several models have been proposed to express $\overline{F}_p$ as a function of the relative displacement between the colliding systems, either considering a linear or a nonlinear force relation, and with or without a viscous damper [34,43,44]. Still, even though the nonlinear force-based approach is more accurate in terms of simulating the real behaviour, the linear viscous model has been found to be more efficient for computationally-intense applications such as performance-based studies due to its balance between simplicity and accuracy [34,43,70]. Therefore, the model used herein to simulate the pounding behaviour between the considered structures combines a viscous damper and a linear spring with a stiffness defined according to the characteristics of the interacting structures, as proposed by [71] and shown in Figure 8. According to this model, which is also known as the Kelvin–Voigt model, the pounding force $\overline{F}_p$ is expressed as:

$$\overline{F}_p = \begin{cases} \overline{k}(u_x - u_y - G) + \overline{c}(\dot{u}_x - \dot{u}_y) & at\ u_x - u_y > G \\ 0 & at\ u_x - u_y \leq G \end{cases} \quad (2)$$

where G is the separation distance between the colliding structures, and $\overline{k}$ and $\overline{c}$ are the impact stiffness and damping, respectively.

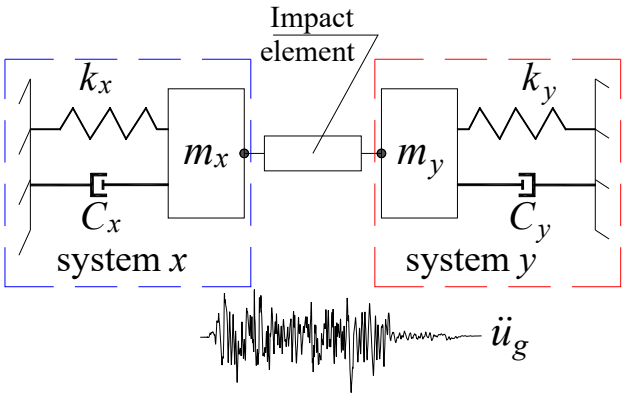

Figure 7. Representation of the model of two structural systems that can collide under earthquake excitation.

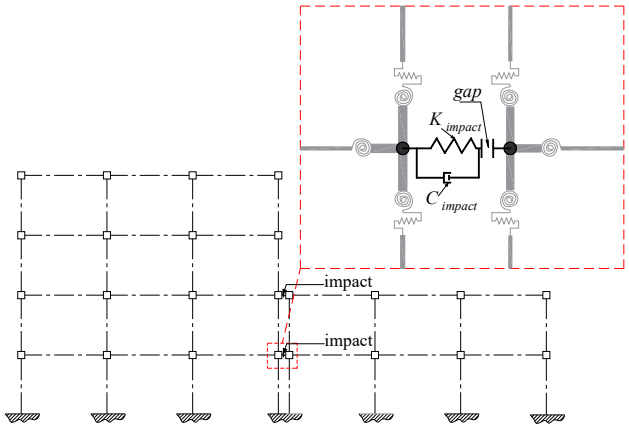

Figure 8. Representation of the contact element model illustrated for a scenario of floor-to-floor impact.

Most of the existing research on the simulation of pounding effects in buildings relates the contact stiffness either with the axial stiffness or the lateral stiffness of the colliding

buildings, with or without using a dynamic amplification factor γ [69,70,72]. Due to the absence of relevant large-scale experimental data, the variability of values that have been assigned to the impact stiffness in past research is large [19,32,70]. Nevertheless, it has been observed that, within a given range, using different impact stiffness values has either a minor or no effect on the results, e.g., see [15,73]. This fact was confirmed in the current study following preliminary analyses carried out using different impact stiffness values defined as an amplified value of the lateral stiffness of the structures. It was concluded that, for the considered buildings, using an amplification factor γ based on a lateral stiffness with a value of 10 or higher allows simulating the interaction between the structures without excessive penetration between the contact nodes. However, given the high nonlinearity effects involved in the contact problem, along with the fact that shear springs are included in the structural models, using a large impact stiffness (larger than 20 times the lateral stiffness) can lead to numerical instability and increases the computational cost since it requires infinitesimal time steps. Therefore, a value of γ equal to 10 was used herein. In terms of the damping coefficient $\bar{c}$, its value is estimated based on the coefficient of restitution (e) and its relation with the energy dissipation during the impact [71,74] using:

$$\bar{c} = 2\zeta\sqrt{\bar{k}\left(\frac{m_x m_y}{m_x + m_y}\right)} \text{where} \zeta = -\frac{\ln e}{\sqrt{\pi^2 + (\ln e)^2}} \quad (3)$$

A value of 0.65 was found to be the most recommended value for the coefficient of restitution (e) [75–78], which corresponds to a value of ζ equal to 0.135.

Finally, it should be noted that, given the complexity of the pounding phenomenon, the formulations that are used to compute the impact stiffness and the damping coefficient for defining the pounding forces can be considered to be simplified models. For example, the formulations do not account for factors that may have an influence on the pounding forces such as the effect of damage concentration at the contact area, uncertainty about the geometry of the contact area, or uncertainty about the masses that contribute to the impact [79]. However, since previous research has shown that using different impact stiffness and damping coefficient values has a minor influence on the global response of the structure (e.g., see [19,73,77]), the referred formulations are expected to provide adequate values for the analyses that were performed.

4.3. Incremental Dynamic Analysis and Ground Motion Selection

The seismic behaviour of the considered structures was analysed using IDA [49]. IDA considers the response variability due to record-to-record variability by analysing a structural model subjected to n ground motions, each one scaled to multiple levels of intensity. As an output, IDA produces n curves representing the evolution of a selected structural response parameter as a function of the ground motion intensity levels measured by a given intensity measure (IM). In order to use a uniform IM across all the structures and pounding configurations analysed herein, the considered IM is the mean of the log of the 5%-damped spectral acceleration at periods between 0.15s and 1.5s (AvgSa) [80]. Using this IM ensures increased efficiency and (relative) sufficiency in estimating a given structural response parameter when using a scalar IM [81,82].

The IDAs of each structure were carried out using fifty real ground motion records selected to match a target response spectrum. The selected target response spectrum that defines the reference seismic scenario corresponds to that of Zone 3 of the Egyptian territory, considering the Type 2 elastic response spectrum and a soil of type B according to the Egyptian design code [18]. The peak ground acceleration associated with this scenario is 0.15 g, which corresponds to a return period of 475 years. The ground motion records were selected from the NGA-WEST2 database [83] in order to be compatible with the referred scenario. The records are characterised by magnitudes higher than 5.5 and epicentral distances larger than 10 km. The selected ground motion records were scaled to match the target response spectrum of Zone 3 of the Egyptian territory according to the procedures

described in [84] in the range of periods between 0.15 s and 1.5 s, which covers all the fundamental periods of the selected structures [85]. The scaling factors that were used for the spectral matching range from 0.3 to 2.4. Figure 9 shows the elastic response spectra of the fifty ground motion records along with their mean response spectrum and the target response spectrum. A list of the selected ground motions, along with their characteristics, is provided as a Supplementary File (Table S1).

The structural parameter selected herein to measure the response of the structures is the maximum interstorey drift over the height $\bar{\theta}_{max}$. Moreover, structural performance was analysed for different limit states describing the state of the structure according to predefined levels of damage, e.g., the onset of cracking, yielding, collapse. Although a significant amount of research has been carried out over the years addressing the definition of drift-related limit states for RC buildings (e.g., see [86–90] among several others), the values proposed by FEMA-356 [89] are considered herein given their wide acceptance. These values are 1%, 2%, and 4%, which correspond to limit states of immediate occupation (IO), life safety (LS), and collapse prevention (CP), respectively. Additionally, a limit state representing the initiation of cracks (CI) was also considered and for which a drift limit of 0.50% was assigned. The expected (i.e., desired) damage for the latter limit state (i.e., CI) assumes that hairline cracks have developed in RC elements due to excessive tensile stress and that no elements have yielded. The expected damage for the remaining limits states considers the assumptions of FEMA-356 [89]. For the immediate occupation (IO) limit state, the physical damage corresponds to hairline cracking in RC elements and the yielding of a few elements without concrete crushing. For the life safety (LS) limit state, the physical damage is expected to involve extensive damage to RC elements with concrete spalling, shear cracking, and joint cracking. Globally, the structure still has some reserve of lateral strength and stiffness, and a ductile collapse mechanism may not be fully developed. Finally, collapse prevention (CP) represents a damage state where a global collapse mechanism is expected to be fully formed and the structure is likely to have a low residual lateral strength and stiffness, meaning that extensive damage has spread across all the critical RC elements and joints and that the structure is near collapse. To trace the performance of the considered structures for increasing levels of demand using IDA, the input ground motions were incrementally scaled up to levels where the global failure of the structures is reached. The global failure of a given structure is assumed to happen when dynamic instability (nonconvergence) of the numerical model occurs [63]. This nonconvergence occurs when interstorey drifts increase without bound due to either the occurrence of large flexural deformations or a significant number of shear failures. In addition, when the value of $\bar{\theta}_{max}$ reached by a structure exceeds the value of 4% (the limit value for CP), a state of global failure is also assumed for the structure.

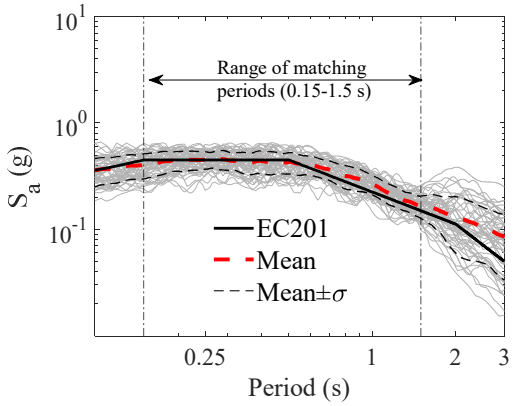

Figure 9. Scaled response spectra for the fifty ground motions with their mean response spectrum and the target elastic response spectrum for Zone 3 of the Egyptian territory according to the Egyptian code for loads EC201 (Type 2 design response spectrum and Soil B).

4.4. Probabilistic Definition of the Separation Distance between the Buildings

As mentioned before, design codes and specifications recommend the implementation of a separation distance between adjacent buildings as a measure to mitigate pounding effects [37]. Still, these recommendations vary in the way the separation distance should be determined. For example, some standards estimate the separation distance G by combining the elastic response of the adjacent buildings using different combination rules (e.g., the square root sum rule is used in [91] while the square root of the sum of the squares (SRSS) rule is used in [18,92]). Others correlate the separation distance using the buildings' height [93], in which adjacent buildings need to be separated by a distance corresponding to 1% of the adjacent buildings' height. These various definitions lead to a wide range of possible separation distance values. This variety can be interpreted as being related to the underlying uncertainty associated with the earthquake excitation.

To address this issue, the proposed study uses a probabilistic approach that accounts for the record-to-record variability for defining reference values of the separation distance. The primary purpose of these reference values is not to avoid the occurrence of pounding. Instead, different ratios of these values are used in the analyses to understand their effect on the probabilistic performance of the structures for different limit states. The selected separation distance values are estimated based on the elastic response of the structures subjected to the set of ground motions compatible with the elastic response spectrum. Although the selected ground motions were previously scaled to match the target response spectrum across a period range of 0.15–1.5s, the linear dynamic analyses performed for each structure considered the ground motions scaled to match the target spectrum at the fundamental period of the structure, as shown in Figure 10. This different scaling approach was used to minimise the record-to-record variability of the response of each individual structure.

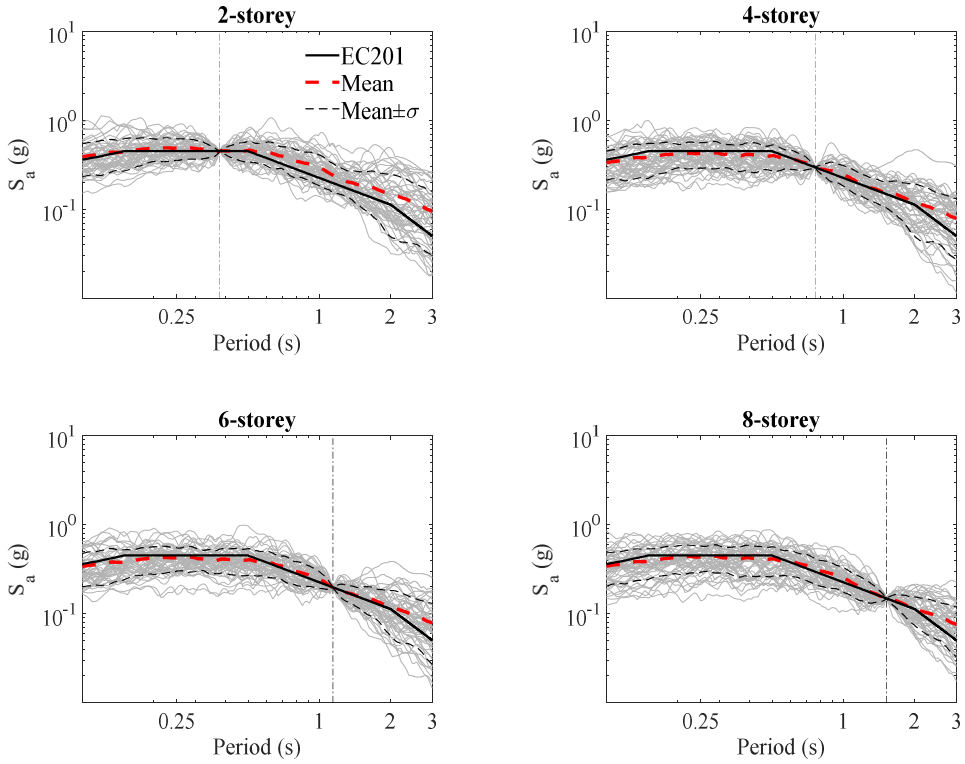

Figure 10. Scaled response spectra for the fifty ground motions with their mean response spectrum and the target elastic response spectrum for Zone 3 of the Egyptian territory according to the Egyptian code for loads EC201 (Type 2 design response spectrum and Soil B) at four different periods.

Histograms representing the distribution of the maximum elastic displacements (δ) of several storeys of the considered buildings are plotted in Figure 11 (diagonal and lower diagonal plots). In addition, scatter plots are also presented in Figure 11 (upper diagonal plots) showing the maximum top displacement obtained for a given structure along with the corresponding maximum displacement obtained at that same level in taller structures. The results show that, even when scaling the records to match the target response spectrum at the fundamental period of each structure, their elastic response exhibits a non-negligible dispersion characterised by a coefficient of variation (CoV) which ranges from 12.5% to 14.9%. Moreover, Figure 11 (upper diagonal plots) shows that, as expected, the correlation between the lateral displacement of structures with different heights but measured at common levels is imperfect (due to several factors, namely the frequency content of the different ground motions). In this comparison, the response of structures with a higher number of storeys tends to be larger, but the differences tend to be smaller when comparing displacements of structures with a number of storeys that is closer. For example, when comparing the displacement of the 8-storey structure at the second and sixth levels with the top displacements of the 2-storey and 6-storey structures, respectively, the latter comparison exhibits a smaller difference than the former. Based on these results, the reference value of the separation distance considered for each pair of adjacent buildings analysed herein was estimated from the SRSS of the mean values of the maximum displacements of the two buildings at the level corresponding to the height of the shorter building. Table 1 provides the matrix of the mean μ and CoV values of the lateral displacement of each structure at the levels relevant for the pounding analyses, along with the reference value of the separation distance (G) computed for each pair of adjacent buildings using the referred SRSS rule. In addition, Table 1 also presents the spectral displacement Sd obtained for each structure based on the elastic target response spectrum. As can be seen, Sd is close to the corresponding mean value of the lateral displacements obtained from the selected ground motions, which reflects the adequacy of the ground motion selection process.

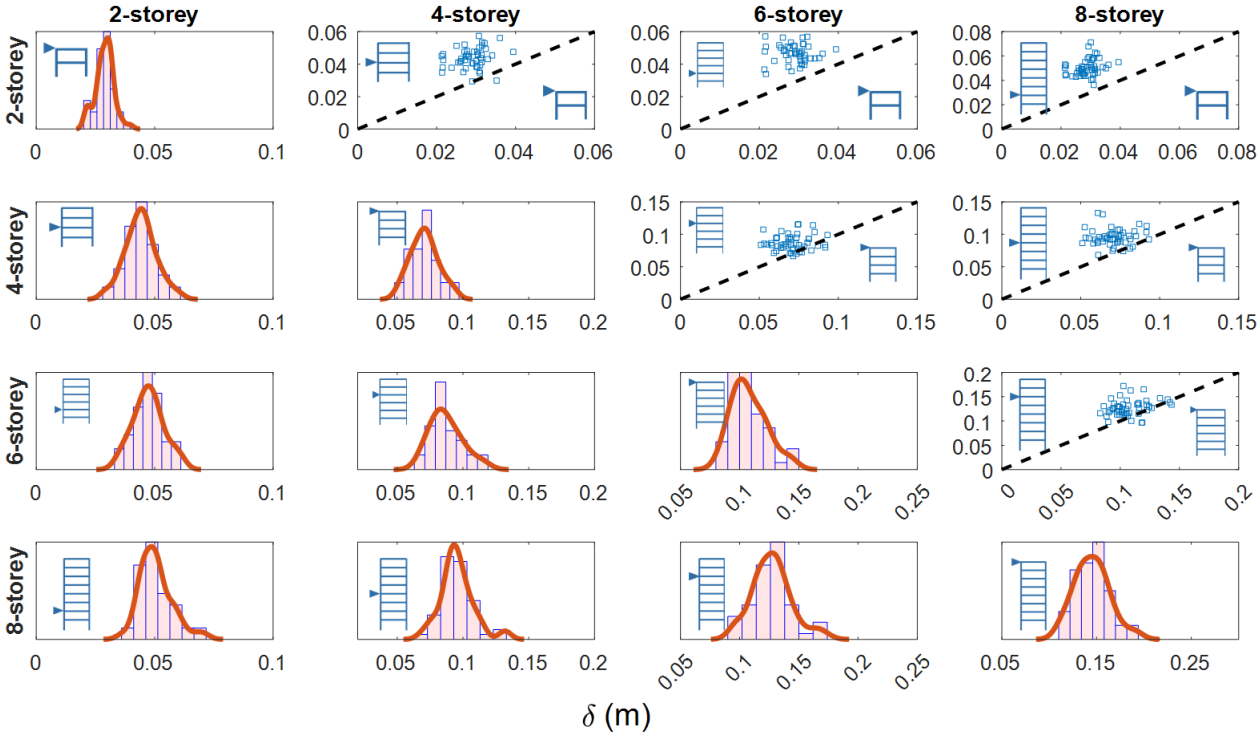

Figure 11. Histograms (diagonal and lower diagonal plots) of the maximum displacement at several storeys, and scatter plots (upper diagonal plots) of the maximum top displacement obtained for a given structure along with the corresponding maximum displacement obtained at that same level in taller structures.

Table 1. Statistics of the lateral displacement of the structures at different levels obtained from dynamic analyses, spectral displacement of the structures, and reference values G of the separation distance for pairs of adjacent buildings.

Main Building	Sd (m)	2-Storey		4-Storey		6-Storey		8-Storey		$G=\sqrt{\mu_x^2+\mu_y^2}$			
		μ	CoV (%)	μ (m)	CoV (%)	μ (m)	CoV (%)	μ (m)	CoV (%)	Adjacent Building			
										N2	N4	N6	N8
N2	0.020	0.029	13.1							0.041	0.053	0.055	0.058
N4	0.067	0.044	14.9	0.071	14.6							0.11	0.12
N6	0.11	0.047	13.6	0.087	13.8	0.11	13.5						
N8	0.15	0.050	13.6	0.096	13.1	0.13	12.9	0.15	12.5				

4.5. Considered Pounding Configurations

Among the more vulnerable building configurations previously referred to (see also [9,13,15,21]), the present study analyses several scenarios that are relevant for regional or city-scale seismic risk assessment studies. These scenarios involve floor-to-column pounding, floor-to-floor pounding, pounding between buildings with a significant height difference, and pounding between buildings with a significant mass difference. The scenario involving adjacent buildings with different heights is simulated by analysing the pounding effects between two reference frames with a different number of storeys. On the other hand, the scenario involving adjacent buildings with different masses is simulated by analysing the pounding effects between one reference frame and a second frame with a much larger number of bays with characteristics similar to those of a reference frame with the same height. Figure 12 shows representative examples of the considered pounding configurations along with the parameters that define them. Table 2 details all the considered pounding configurations and their corresponding characteristics, including the different values of the separation distance and shift distance (see Figure 12a) that were considered.

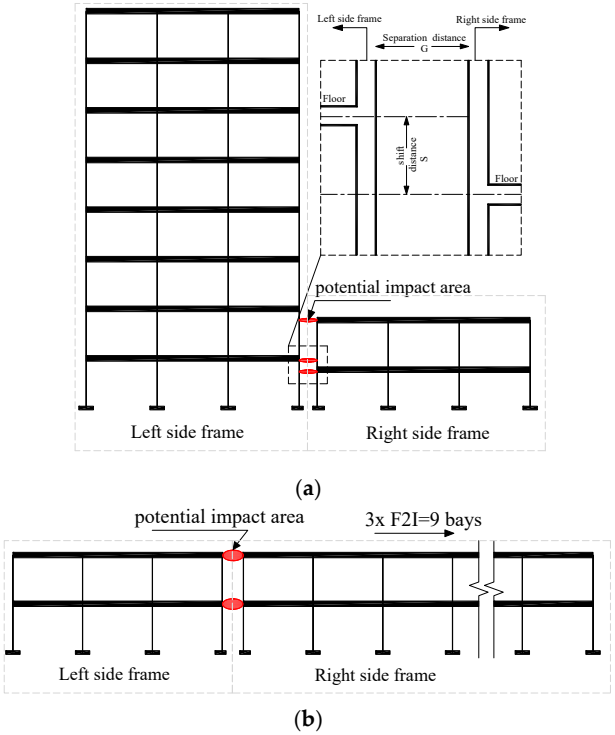

Figure 12. Example of a pounding configuration involving structures with significantly different heights (**a**) and a pounding configuration involving structures with significantly different masses (**b**). (**a**) Pounding configuration involving an 8-storey frame adjacent to a 2-storey frame with floor-to-column contact (F8PS2G0). (**b**) Pounding configuration involving a 2-storey frame adjacent to an extended version (with nine bays) of the 2-storey frame (F2PE2G0).

Table 2. Characteristics of the considered adjacent structures representing the different critical pounding configurations (■ marks the selected characteristics of a given pounding configuration).

No.	Left Side Frame ‡	Right Side Frame	Shift Distance S (m) (Figure 12a)	Separation Distance	Acronym *	Pounding Configurations			
						Type of Pounding		Adjacent Buildings with Significantly Different	
						Floor-to-Floor	Floor-to-Column	Masses	Heights
1	4-Storey	2-Storey	0.0	G0.0	F4P2G0.0	■			
2	6-Storey	2-Storey	0.0	G0.0	F6P2G0.0	■			
3	8-Storey	2-Storey	0.0	G0.0	F8P2G0.0	■			■
4	6-Storey	4-Storey	0.0	G0.0	F6P4G0.0	■			■
5	8-Storey	4-Storey	0.0	G0.0	F8P4G0.0	■			■
6	4-Storey	2-Storey	0.50	G0.0	F4PS2G0.0		■		
7	6-Storey	2-Storey	0.50	G0.0	F6PS2G0.0		■		■
8	8-Storey	2-Storey	0.50	G0.0	F8PS2G0.0		■		■
9	6-Storey	4-Storey	0.50	G0.0	F6PS4G0.0		■		
10	8-Storey	4-Storey	0.50	G0.0	F8PS4G0.0		■		■
11	2-Storey	2-Storey (extended 3x)	0.0	G0.0	F2PE2G0.0	■		■	
12	4-Storey	2-Storey (extended 3x)	0.0	G0.0	F4PE2G0.0	■		■	
13	6-Storey	2-Storey (extended 3x)	0.0	G0.0	F6PE2G0.0	■		■	■
14	8-Storey	2-Storey (extended 3x)	0.0	G0.0	F8PE2G0.0	■		■	■
15	4-Storey	2-Storey	0.50	G0.5	F4PS2G0.5		■		
16	6-Storey	2-Storey	0.50	G0.5	F6PS2G0.5		■		■
17	8-Storey	2-Storey	0.50	G0.5	F8PS2G0.5		■		■
18	6-Storey	4-Storey	0.50	G0.5	F6PS4G0.5		■		
19	8-Storey	4-Storey	0.50	G0.5	F8PS4G0.5		■		■
20	4-Storey	2-Storey	0.50	G1.0	F4PS2G1.0		■		
21	6-Storey	2-Storey	0.50	G1.0	F6PS2G1.0		■		■
22	8-Storey	2-Storey	0.50	G1.0	F8PS2G1.0		■		■
23	6-Storey	4-Storey	0.50	G1.0	F6PS4G1.0		■		
24	8-Storey	4-Storey	0.50	G1.0	F8PS4G1.0		■		■
25	6-Storey	4-Storey	0.0	G0.5	F6P4G0.5	■			■
26	8-Storey	4-Storey	0.0	G0.5	F8P4G0.5	■			■
27	4-Storey	2-Storey	0.0	G1.0	F4P2G1.0	■			
28	6-Storey	2-Storey	0.0	G1.0	F6P2G1.0	■			
29	8-Storey	2-Storey	0.0	G1.0	F8P2G1.0	■			■
30	6-Storey	4-Storey	0.0	G1.0	F6P4G1.0	■			■
31	8-Storey	4-Storey	0.0	G1.0	F8P4G1.0	■			■

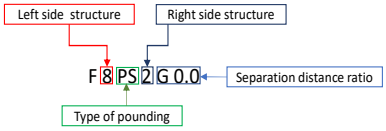

* P stands for floor-to-floor pounding; PS stands for floor-to-column pounding; Gx is the separation distance defined as a ratio of the value in Table 1 for the structures of a given configuration; PE stands for pounding involving an extended frame (i.e., one of the frames has a significantly different mass); ‡ The taller structure is always the left-hand side structure.

5. Behaviour of the Analysed Structures

5.1. Capacity Curves and IDA Curves of the Control Cases

To better understand the overall performance of the structures selected as control cases, the corresponding capacity curves obtained from pushover analyses [94] using a first-mode-proportional lateral load pattern are presented in Figure 13. The base shear values presented for each structure are normalised by the weight of the corresponding structure and the lateral deformation is represented by the top storey drift. Given the gravity design of the considered structures, buildings with a lower number of storeys tend to have higher normalised shear capacity and ductile behaviour when compared to those with a higher number of storeys. By considering the location of the considered structures (see Section 4.3), it is noted that designing these structures for earthquake loading would lead to a ratio between the base shear and the weight of the structures (i.e., the lateral load coefficient discussed in [95]) of 0.11~0.12g. By comparing these values with the capacities represented in Figure 13, it can be seen that only the 2- and 4-storey structures are able to reach that level of seismic demand. This is mostly due to the minimum conditions enforced by the design code for gravity design [18], namely those addressing the size of the member cross sections and the longitudinal reinforcement ratio, which are particularly conservative.

In addition to these results, the IDA curves of the control case structures obtained for the previously referred fifty ground motions are also presented in Figure 14. Each curve represents the evolution of $\bar{\theta}_{max}$ (the maximum inter-storey drift over the height of the structure) for increasing values of the IM (AvgSa). Each IDA plot also presents the corresponding median IDA curve along with the 16th and 84th percentile curves. These IDA curves can then be compared with the IDA curves obtained for the different arrangements of adjacent buildings. Figure 15 presents pairs of IDA curve plots for some of the selected pounding configurations (the full 31 pairs of IDA curve plots are provided in Figure S1 of the Supplementary file). The 68% confidence interval of the IDA curves obtained for the

corresponding control case of each structure involved in a given pounding configuration is also represented in the background of the IDA curves to facilitate the qualitative comparison between the different configurations i.e., structures with/without pounding effects. In addition, the first shear failure occurring in a column of a certain structure for a given ground motion is also identified in the corresponding IDA curve by a red star-shaped marker, while the global failure of the adjacent structure is identified by a blue dot marker. From these results, it can be seen that when the shear failure of a column occurs, it triggers the subsequent failure of other columns, which then rapidly leads to the global failure of the structure for that IM value or one involving an infinitesimal IM increment.

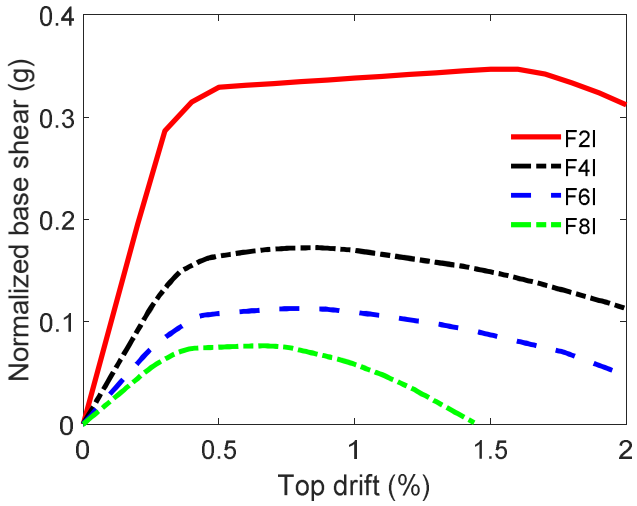

Figure 13. Capacity curves of the different control case structures obtained from pushover analyses.

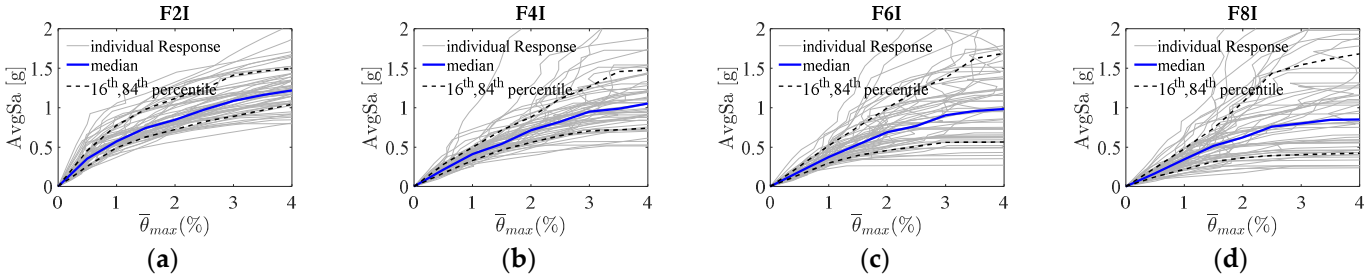

Figure 14. IDA curves obtained for the control case structures: (**a**) structure F2I, (**b**) F4I, (**c**) F6I and (**d**) F8I.

The results of the cases shown in Figure 15 also highlight that the several pounding configurations involving floor-to-floor contact between the buildings, either with or without a separation distance, do not exhibit a significantly different performance. On the other hand, when compared to these configurations, those involving floor-to-column contact exhibit a significant number of shear failures. For these configurations, having a larger separation distance between the adjacent structures provides better performance, but the occurrence of shear failures is inevitable for the considered configurations. Since all the structures were only designed for gravity loads, the global failure of a given pounding configuration can be seen to be mostly driven by the failure of the taller structure involved in the configuration. Furthermore, for the range of IM values involved in the analyses, structures with a lower number of storeys generally exhibit a similar behaviour across the different pounding configurations.

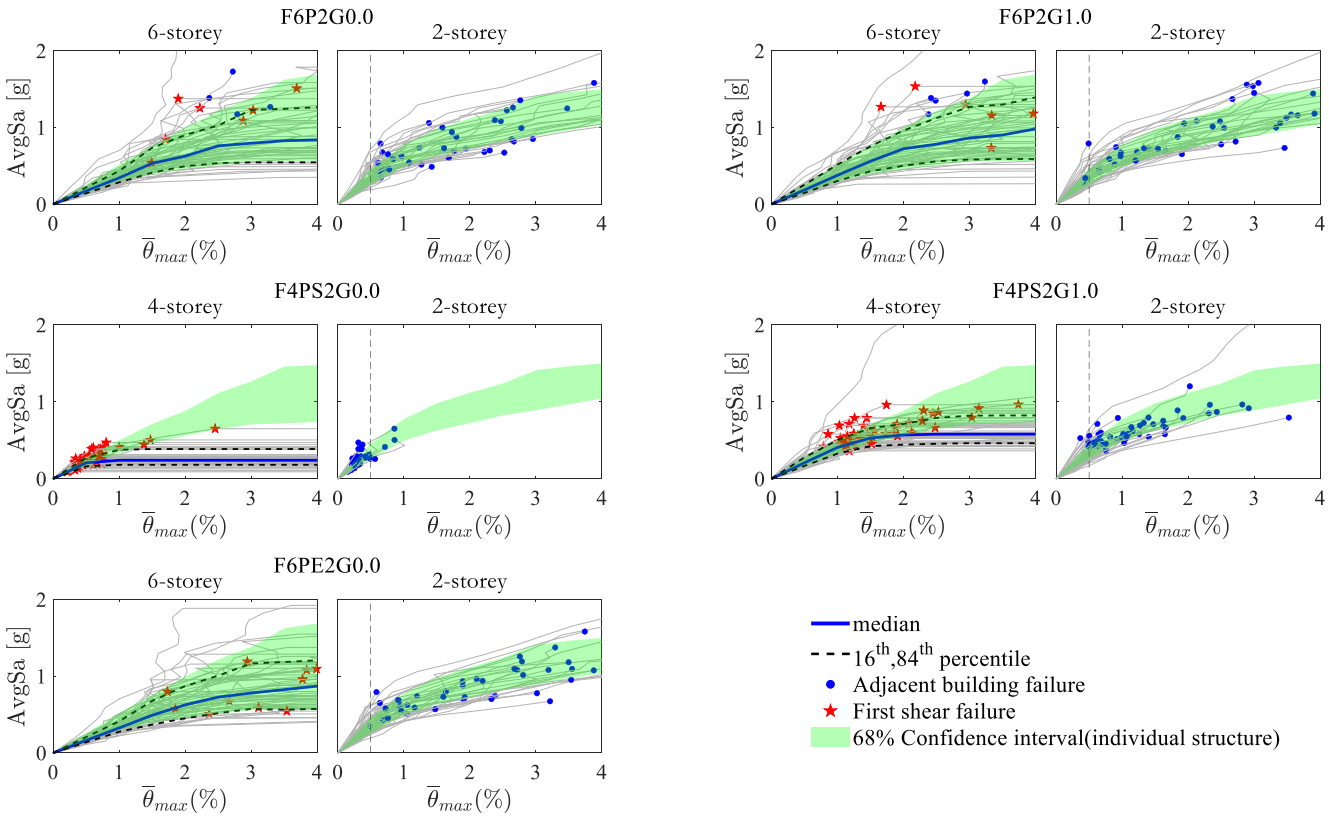

Figure 15. IDA curves obtained for some of the pounding configurations.

5.2. Failure Mechanisms Observed for Different Pounding Configurations

As referred to before, pounding leads to different dynamic responses of the structures that are involved and, therefore, to different failure mechanisms. Moreover, when pounding occurs, the impact force created by the collision is the parameter that governs the structural behaviour. The impact force exerts a stress pulse that travels from the impact point to the different elements of the impacted structure. Therefore, this stress pulse plays a key role in the overall behaviour of the impacted structure and on its failure mechanism. Furthermore, the ability of the structure to sustain such a level of force over a short time interval depends on the load path this force will travel through the structure starting from the impact point. As such, the floor alignment plays a key role in the overall structural performance of the impacted buildings and, eventually, on their failure mechanism. As shown in Figure 16, when the impact occurs between structures with aligned floors leading to floor-to-floor contact, the load path of the impact force starts from an element with a large axial stiffness (i.e., the floor), which is able to distribute the impact force across the connected columns. On the other hand, when floor-to-column pounding is involved, the impact force needs to first pass through the pounded columns before reaching the floor (see Figure 16). As such, this type of pounding mechanism is more likely to lead to a global failure mechanism governed by the shear failure of columns, as confirmed by the results discussed in the previous section. Nevertheless, both types of pounding mechanisms can lead to global failure driven by the shear failure of columns. In the case of floor-to-column configurations, shear failure is likely to occur at the level of impact, while in the case of floor-to-floor pounding configurations, it is likely to occur above the contact level.

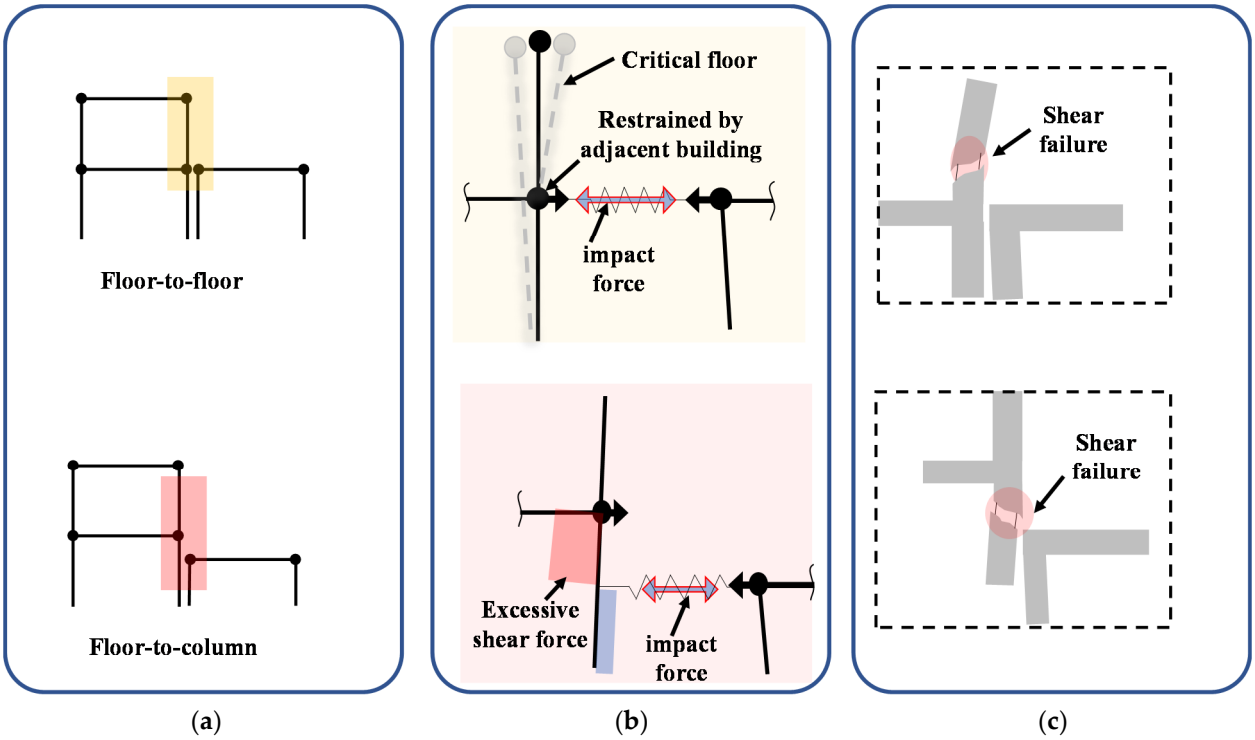

Figure 16. Illustration of the type of shear failure associated with each type of pounding configuration: (**a**) pounding configuration, (**b**) load path and (**c**) observed shear failure.

Despite the greater possibility of occurrence of shear failure when pounding is involved, the number of cases in which failure is driven by flexural failure of columns is still significant for certain pounding configurations. Overall, examining the analysis results at the structural element level when global failure of a given structure occurs highlights that one of the following two categories of failure are more likely to happen: flexural failure of columns at a level above the pounding-level columns, or shear failure of columns at the level of impact or above. In terms of the shear failure, depending on the state of the spring elements simulating the inelastic behaviour in flexure, this failure can be classified as a flexural-shear failure (when the column has yielded) or a pure shear failure (when the column has not yielded) (see Figure 5). To illustrate these findings, Figure 17 shows the percentage of each type of failure mechanism found for some of the considered structures by analysing the state of all the columns that are involved in the global failure of each structure for each IDA. As can be seen, for the cases involving floor-to-floor contact, the dominant failure mechanism of columns is still the pure flexural failure mechanism, followed by the ductile shear failure mechanism, and pure shear failure. The occurrence of cases where global failure is caused by the shear failure of columns can be interpreted as a direct impact of pounding, since the global failure of the control case structures is always governed by the pure flexural failure of columns. Furthermore, when floor-to-floor pounding is involved, considering larger values of the separation distance can also be seen to have a limited effect in reducing the occurrence of shear failure cases. On the contrary, when floor-to-column pounding is involved, a much larger number of cases of global failure governed by pure shear failure can be seen to occur, and the value of the separation distance has a larger effect on the type of column failure. This conclusion confirms the findings of Karayannis and Favvata [24], where floor-to-column pounding was shown to lead to a significant increase in shear demand and to premature shear failure. As can be seen, when considering larger values of the separation distance, the number of pure shear failure cases is greatly reduced and the dominant failure mechanism becomes flexure-shear, followed by pure flexure.

Even though the pure flexural failure mechanism governs the behaviour when floor-to-floor pounding is involved, the failure patterns that are identified are different from those found for the corresponding control case. Given that the adjacent structure can be thought of as a flexible support for the taller building at the time of impact, the failure of the taller structure is then shifted to a level over the pounding level or above, as shown in Figure 16. To illustrate these findings, Figure 18 shows the percentage of global failure types that occur at pairs of storeys along the height of a structure for different pounding configurations and control cases. For structures involving pounding, the likelihood of having a critical storey (the storey that governs the global failure mechanism) above the pounding level increases, while the control case structures are more likely to have a critical storey at one of the bottom storeys. Furthermore, the number of cases in which the critical storey is located above the pounding level is also greater when the stiffness of the adjacent structure is larger, as can be seen from the first pounding configuration in each plot that corresponds to a case that simulates pounding between buildings with a significant mass difference. Globally, it can be seen that a larger difference between the heights of adjacent buildings increases the chance of failure of the taller building at a level above the height of the shorter building.

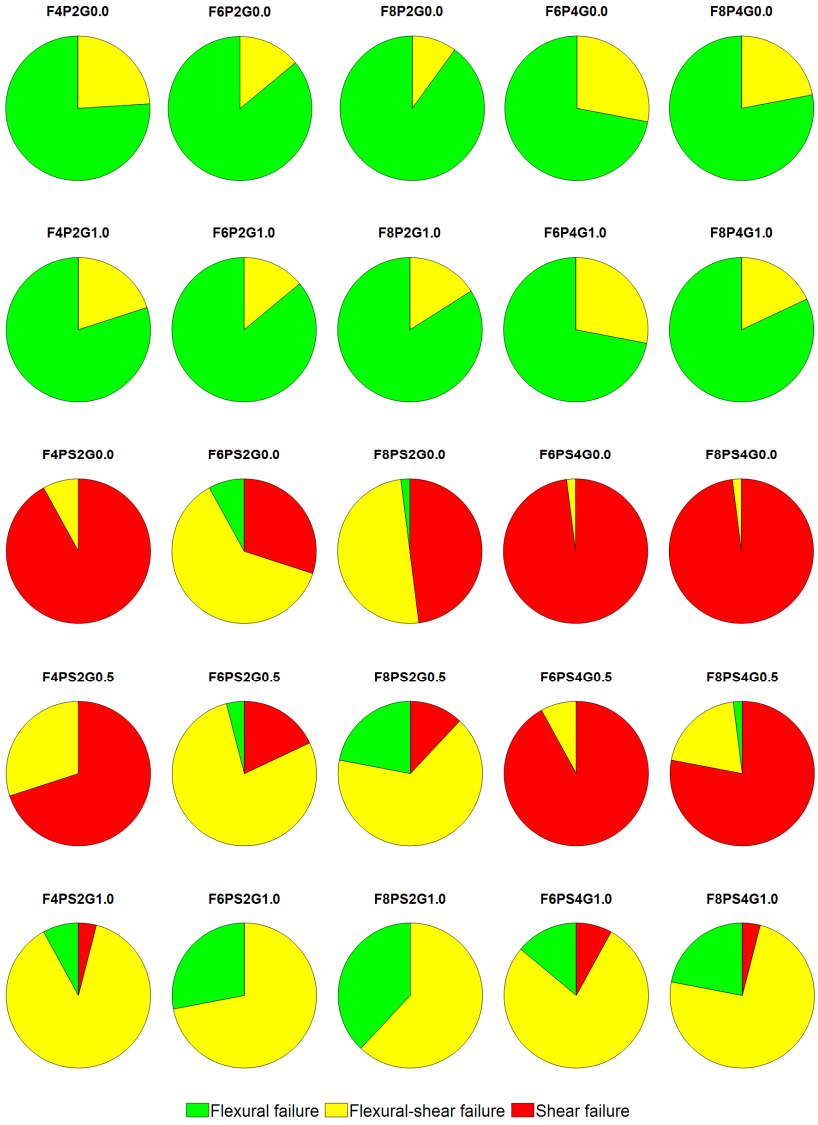

Figure 17. Distribution of types of failure mechanisms for some of the considered pounding configurations.

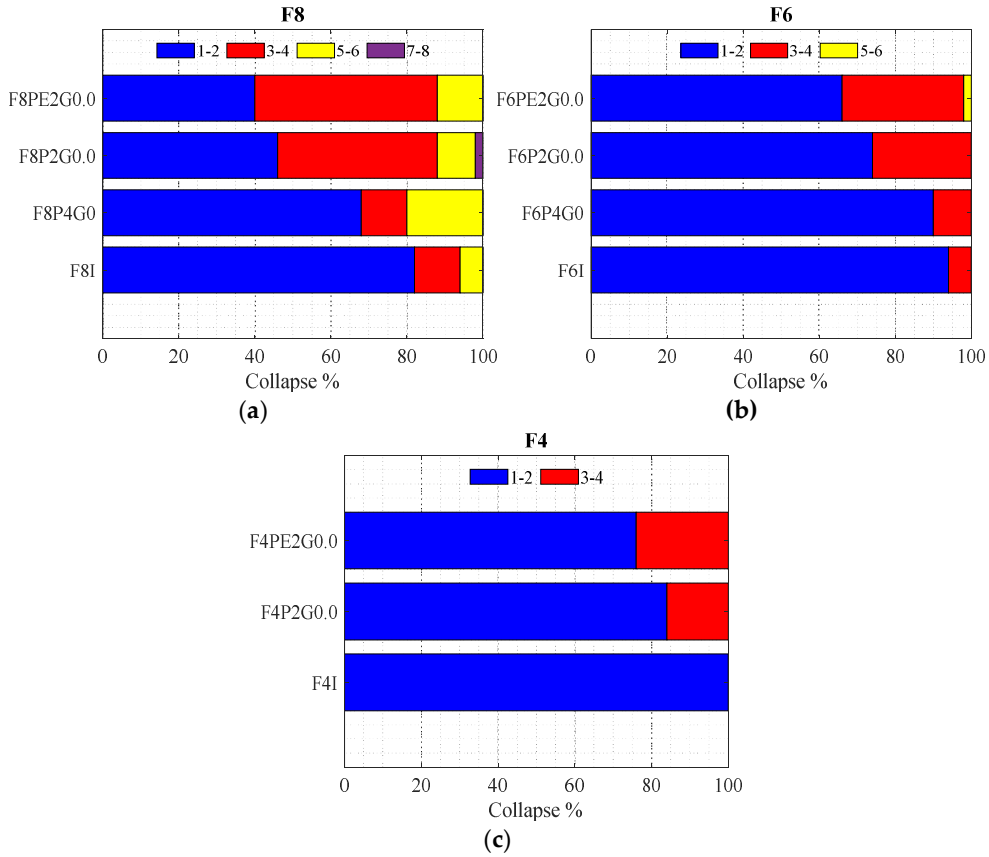

Figure 18. Percentage of global failure mechanisms along the height for different types of structures and pounding configurations: (**a**) all cases involving 8 storey structures, (**b**) all cases involving 6 storey structures and (**c**) all cases involving 4 storey structures.

6. Probabilistic Performance of the Analysed Structures

The probabilistic performance of the analysed structures was examined by developing fragility functions for different limit states. For a given value of the earthquake IM, the fragility function of a given limit state represents the probability of demand D not exceeding the capacity of the structure C, i.e., $P[D \leq C|IM]$. As referred to before, C and D are expressed in terms of the maximum inter-storey drift along the height of the structure $\overline{\theta}_{max}$, and four thresholds were considered to define limit states representing increasing levels of expected physical damage (see Section 4.3). The fragility functions were developed using an IM-based approach and the necessary IM datasets were obtained by interpolating the IDA curves at the limit state thresholds. For a given limit state, the corresponding fragility function was obtained by fitting a theoretical distribution model to the IM dataset. Even though the lognormal distribution is usually seen as an adequate model to express the distribution of structural demand from individual RC buildings [96,97], no particular results have been found for datasets obtained from analyses involving pounding. Given the larger complexity and variety of behaviour exhibited by the selected structures (i.e., due to the interaction between adjacent structures that gives rise to different types of failure mechanism), the adequacy of the lognormal distribution was first examined.

The goodness-of-fit of the lognormal distribution was analysed for the log of the IM datasets using the Shapiro–Wilk normality test [98,99] for a 5% significance level. The results obtained indicate that the lognormal distribution hypothesis cannot be rejected for the majority of the cases. However, around 6% of the datasets involve one or two data points that depart from the bulk of the data for which the lognormal distribution hypothesis is rejected. In order to illustrate the type of datasets that are involved, Figure 19 presents q–q plots of two groups of datasets and illustrates the corresponding goodness-of-

fit obtained with the lognormal distribution (the red line represents the perfect fit). The first group involves datasets representative of cases for which the lognormal distribution hypothesis cannot be rejected according to the Shapiro–Wilk test, while the second group involves datasets representative of cases for which the opposite conclusion was obtained. As can be seen, the level of departure from the distribution hypothesis exhibited by the second group of datasets is not significantly different from that of the first group, except for one or two data points in the upper tail of the data. Since for most of these datasets, the upper tail data (the larger IM values) are expected to have a smaller contribution to the overall risk and losses of a structure (i.e., the corresponding seismic hazard values are expected to be much lower than those of lower IM values) [100], the lognormal distribution was found to be adequate to represent the fragility functions of all the datasets. Still, to minimise the influence of the larger data points and obtain fitted distributions that are governed by the bulk of the datasets, the parameters of the lognormal distributions were determined using robust statistical estimation methods. Therefore, the fragility functions are represented by a lognormal distribution expressed by:

$$P(D \leq C|IM) = \Phi\left[\frac{ln(IM) - ln(\hat{\theta})}{\hat{\beta}}\right] \quad (4)$$

where $\Phi[]$ is the standard normal cumulative distribution, $ln(\hat{\theta})$ is the mean of the log of the dataset (i.e., the median) determined using the logistic M-estimator [101] (a robust estimator of the central value), and $\hat{\beta}$ is the standard deviation of the log of the dataset determined using the τ-scale estimator [102] (a robust estimator of dispersion). Since the global failure of a given pounding configuration was found to be governed by one of the structures (the taller structure in most cases), the IDA curves of the second structure (the shorter structure in most cases) are incomplete (i.e., they do not represent the performance of the structure up to failure), as can be seen from Figure 15. Therefore, the fragility functions presented herein are only those of the structure that governs the performance of a given pounding configuration.

Figure 20 shows the fragility functions that were obtained for the structures that governed the behaviour of the different pounding configurations when the separation distance was zero. The presentation of the figures is organised based on the number of storeys of the taller structure in the different pounding configurations. In addition, each figure also shows the fragility function of the corresponding control structure. As can be seen, the fragility functions involving the extended structures (that simulate the pounding between buildings with a significant mass difference), i.e., F2P2EG0.0, F4P2EG0.0, F6P2EG0.0, and F8P2EG0.0, show larger fragility values when compared to those of the corresponding control cases. Moreover, the difference between the fragility functions increases as the difference in the height of the buildings of a given pounding configuration also increases. When comparing the performance of the different pounding configurations, it can be seen that configurations involving floor-to-floor pounding exhibit a performance close to that of the control cases, in particular, for the limit states of CI and IO. However, for higher intensity limit states, these structures show a higher fragility than the corresponding control case, which is often governed by the lower level of dispersion that the fragility function exhibits. When analysing the results for the floor-to-column pounding configurations, on the other hand, their fragility is seen to be higher, particularly for the LS and CP limit states, due to the occurrence of shear failures. As shown by the IDA curves (see Figure 15 and the Supplemental file), the vulnerability of these configurations is larger when the adjacent structures have a closer number of storeys. On the other hand, in configurations involving floor-to-floor pounding, larger fragility values are found for the CP limit state when the difference in the number of storeys of the structures involved is greater. Overall, as expected, configurations with no separation distance involving floor-to-column pounding exhibit the worst performance among all the considered configurations due to the significant number of global failure cases governed by the shear failure of columns. Furthermore, it can be

seen that when floor-to-floor pounding is involved, the performance of the structures is worse when the difference in the number of storeys of the structures involved is larger, while the opposite is seen when floor-to-column pounding is involved.

Figures 21 and 22 present the fragility functions of different buildings involving floor-to-floor and floor-to-column pounding, respectively, considering different values of the separation distance ratio (see Table 2) to examine its influence. Additionally, the fragility functions of the corresponding control cases are also presented. As a complement, Figure 23 also shows the evolution of the median of the fragility functions of all the structures and for the four limit states. For structures involving floor-to-floor pounding, since their performance is already close to that of the control case when there is no separation distance (see Figure 21), considering a separation distance does not lead to noticeable differences in performance. On the contrary, for configurations involving floor-to-column pounding, the value of the separation distance is crucial and has a large impact on the global behaviour. For the first limit state (CI), the 4-storey structure shows a similar performance for cases with or without a separation distance. However, for higher limit states, shear demand increases significantly and brittle failure is inevitable. As a consequence, the fragility functions of higher limit states (LS and CP) are almost identical. Still, as shown by the corresponding IDA curves, using a separation distance delays the occurrence of brittle failure and leads to a better performance when compared to the case with no separation distance. Similar conclusions can be drawn for the 6-and 8-storey structures, where it can be seen that, by increasing the separation distance between the pounding buildings, the corresponding fragility functions approach that of the control case. Overall, even though the effect of having an adequate seismic separation distance is more prominent in floor-to-column pounding configurations than in floor-to-floor pounding configurations, both configurations benefit, since it ensures better performance for the structures and reduces the likelihood of their premature failure. To allow a more comprehensive and quantitative analysis of the fragility functions presented herein, Table 3 presents the fragility function parameters for all the considered cases. When analysing the fragility functions obtained for the CP limit state, a comparison between the median of the fragility functions obtained for a given control case and those obtained for the different pounding configurations involving this structure shows that, because of pounding, the median decreases between 5% and 13% when floor-to-floor pounding is involved (with an average reduction of 12%). When floor-to-column pounding is involved, the median decreases between 58% and 80% (with an average reduction of 70%) instead. These reduction rates can be seen to be consistent with the results presented by Flenga and Favvata [47] for this limit state and for the case where the building performance is expressed in terms of interstorey drift, when factoring the fact that the pounding configuration involved in this study is different (the study considers that the adjacent building is fully rigid). Finally, based on the results that were obtained, a recommendation is also established for regional- or city-level seismic risk assessment studies. In situations involving building portfolios for which the possibility of pounding is not negligible, fragility functions accounting for the different pounding configurations should be considered, except in cases involving floor-to-floor pounding. For cases involving this pounding configuration, the results of the current study indicate that the fragility functions developed for buildings without considering pounding are likely to be adequate.

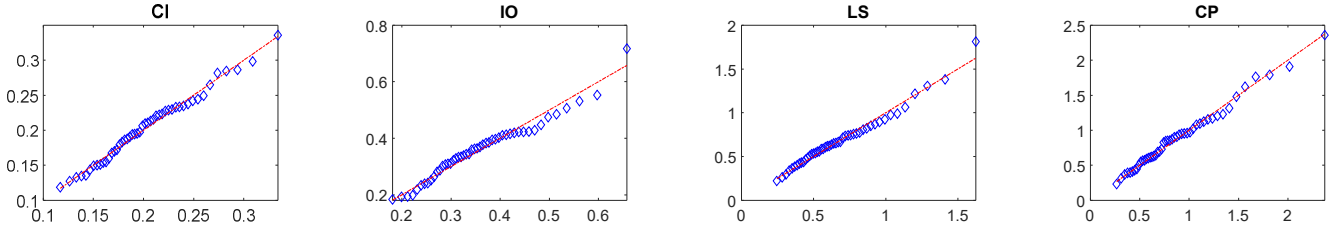

(**a**)

Figure 19. *Cont.*

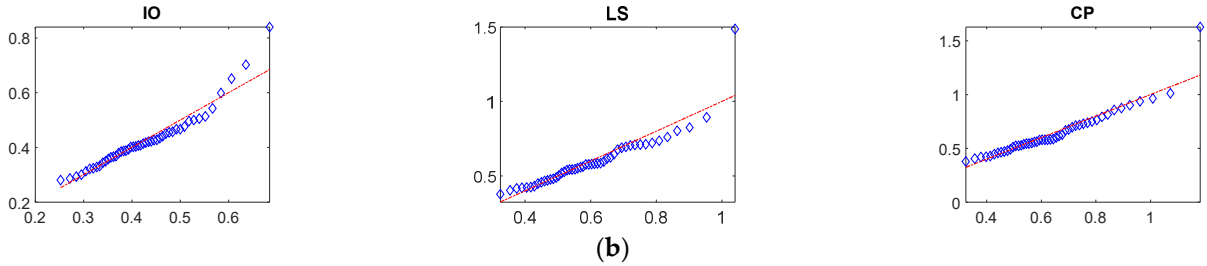

(**b**)

Figure 19. q–q plots of representative IM datasets (all axes are AvgSa in [g]; the horizontal axes are the theoretical quantiles and the vertical axes represent the quantiles of the empirical data): (**a**) datasets representative of cases for which the lognormal distribution hypothesis cannot be rejected—Configuration F8P2G0.0, (**b**) datasets representative of cases for which the lognormal distribution hypothesis is rejected—Configuration F4PS2G1.0.

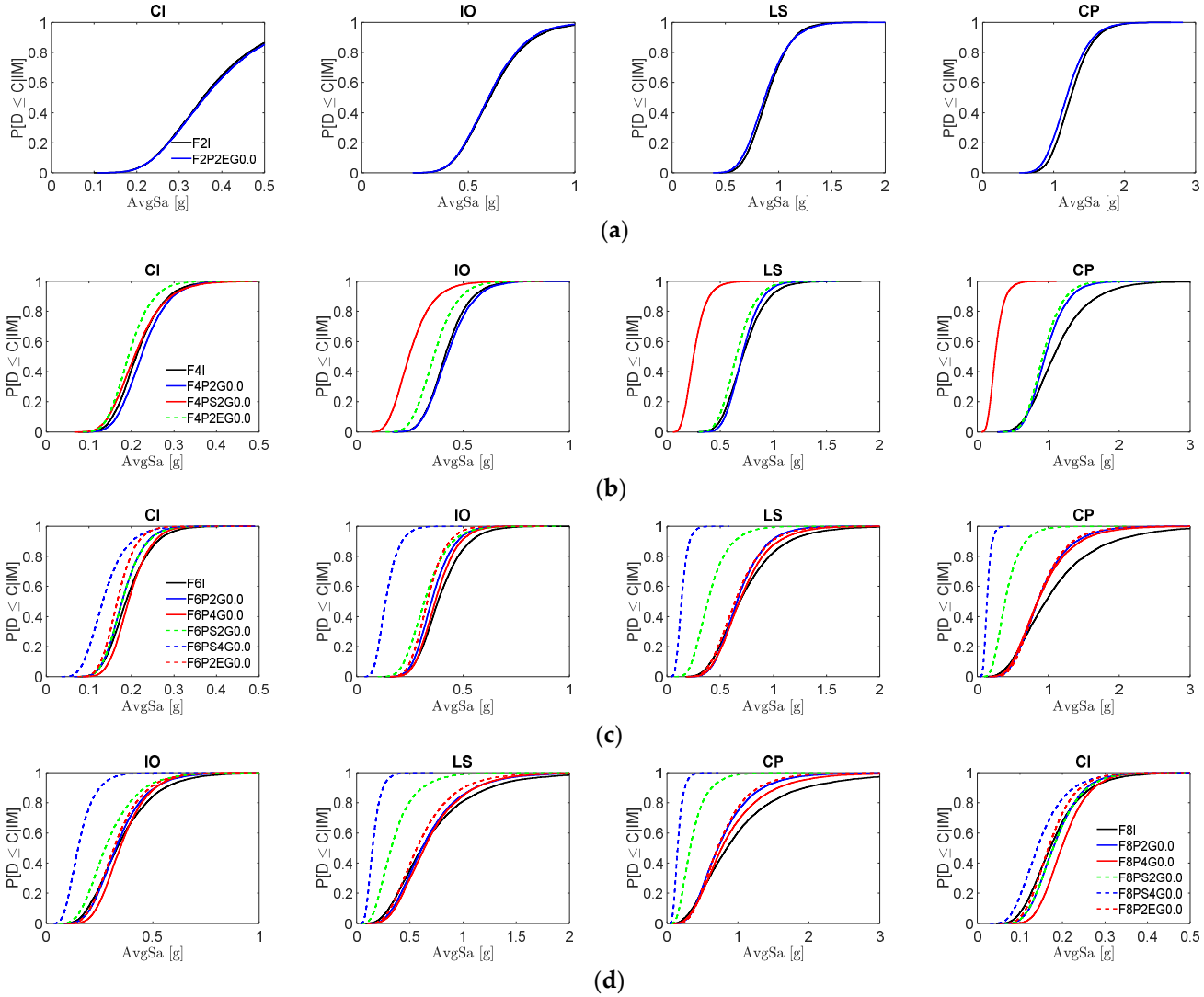

(**a**)

(**b**)

(**c**)

(**d**)

Figure 20. Fragility functions obtained for the different pounding configurations without using a seismic separation distance: cases where the left-hand side structure is a 2-storey structure (**a**), a 4-storey structure (**b**), a 6-storey structure (**c**) and an 8-storey structure (**d**).

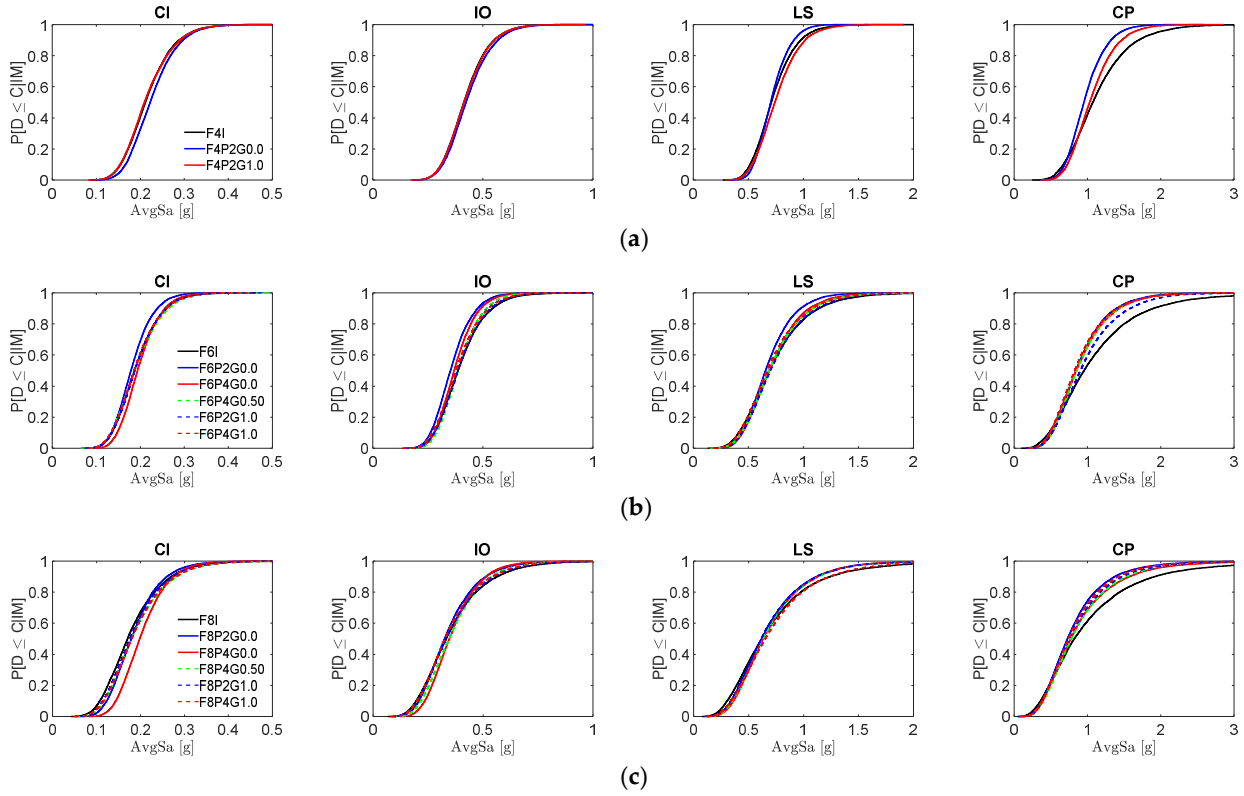

Figure 21. Fragility functions for different structures involving floor-to-floor pounding and different values of the seismic separation distance ratio when the left-hand side structure is a 4-storey (**a**), 6-storey (**b**) and an 8-storey (**c**) building.

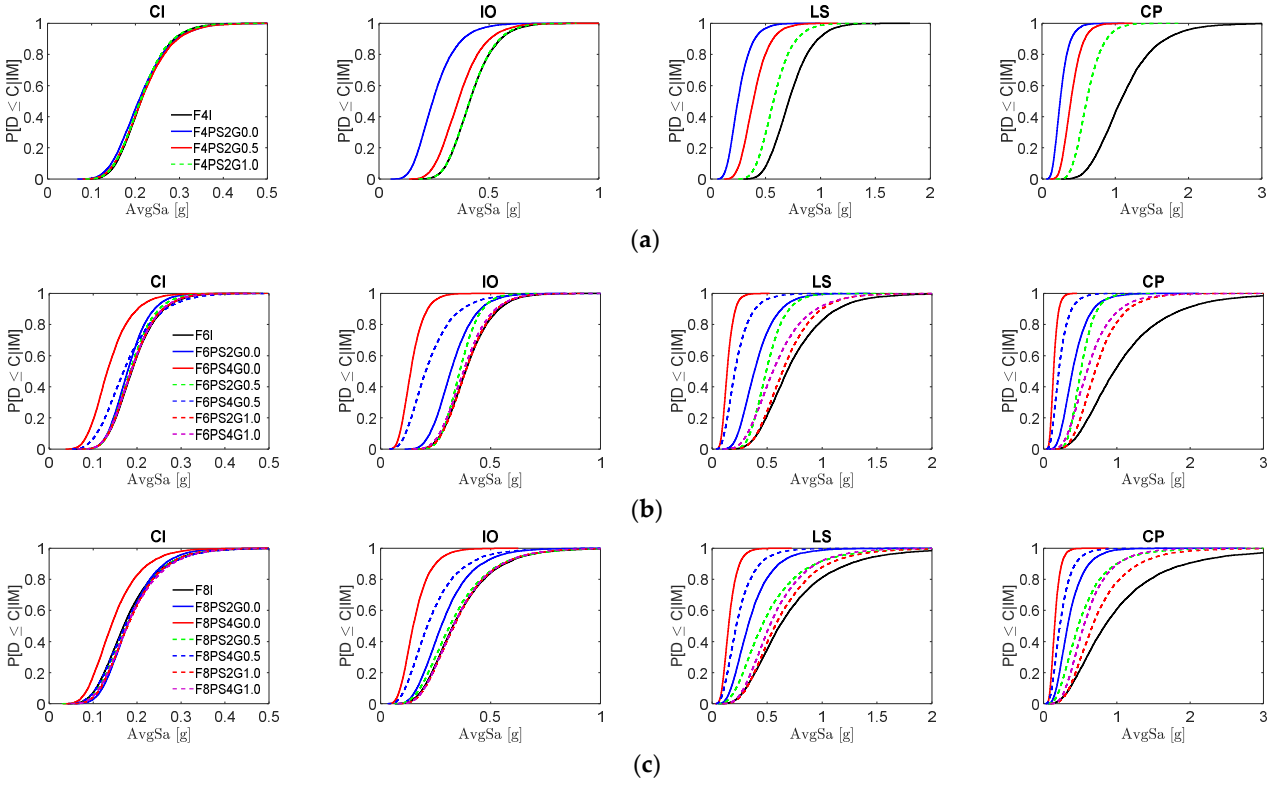

Figure 22. Fragility functions for different structures involving floor-to-column pounding and different values of the seismic separation distance ratio when the left-hand side structure is a 4-storey (**a**), 6-storey (**b**) and an 8-storey (**c**) building.

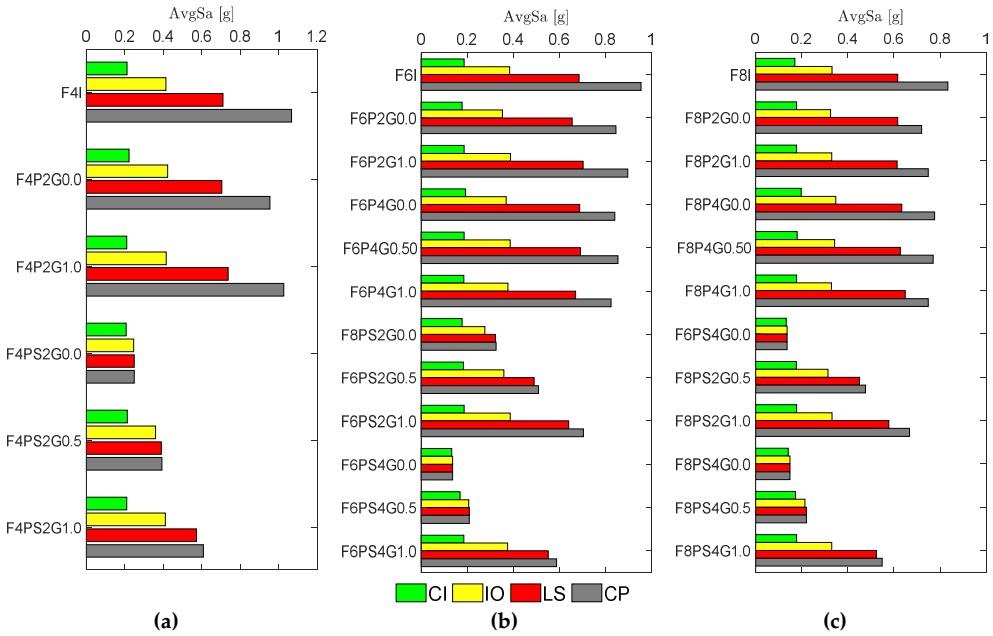

Figure 23. Median of the fragility functions for all the structures and the four limit states: 4-storey (**a**), 6-storey (**b**) and 8-storey (**c**) structures.

Table 3. Parameters of the fragility functions obtained for the different structures.

Model Name	Limit State							
	CI		IO		LS		CP	
	$\hat{\theta}$ [g]	$\hat{\beta}$ [g]	$\hat{\theta}$ [g]	$\hat{\beta}$ [g]	$\hat{\theta}$ [g]	$\hat{\beta}$ [g]	$\hat{\theta}$ [g]	$\hat{\beta}$ [g]
F2I	0.356	0.306	0.599	0.240	0.886	0.205	1.232	0.207
F4I	0.212	0.243	0.414	0.226	0.710	0.248	1.067	0.361
F6I	0.187	0.255	0.385	0.259	0.686	0.396	0.954	0.544
F8I	0.171	0.362	0.332	0.410	0.616	0.543	0.833	0.664
F4P2G0.0	0.222	0.229	0.423	0.230	0.704	0.202	0.955	0.256
F6P2G0.0	0.178	0.228	0.353	0.231	0.656	0.309	0.846	0.395
F8P2G0.0	0.178	0.294	0.325	0.358	0.616	0.465	0.721	0.498
F6P4G0.0	0.193	0.213	0.369	0.222	0.688	0.339	0.841	0.420
F8P4G0.0	0.198	0.254	0.347	0.303	0.634	0.444	0.777	0.548
F4PS2G0.0	0.206	0.276	0.245	0.351	0.248	0.380	0.248	0.380
F6PS2G0.0	0.178	0.233	0.318	0.277	0.384	0.384	0.396	0.429
F8PS2G0.0	0.178	0.300	0.277	0.398	0.323	0.495	0.325	0.501
F6PS4G0.0	0.133	0.321	0.136	0.349	0.136	0.349	0.136	0.349
F8PS4G0.0	0.141	0.370	0.149	0.398	0.149	0.402	0.149	0.402
F2P2EG0.0	0.358	0.317	0.594	0.235	0.872	0.224	1.174	0.224
F4P2EG0.0	0.193	0.225	0.361	0.242	0.649	0.226	0.923	0.240
F6P2EG0.0	0.167	0.206	0.331	0.214	0.639	0.336	0.848	0.371
F8P2EG0.0	0.168	0.289	0.318	0.334	0.566	0.447	0.713	0.472
F4PS2G0.5	0.213	0.260	0.360	0.265	0.389	0.301	0.393	0.313
F6PS2G0.5	0.184	0.243	0.359	0.201	0.491	0.278	0.509	0.295
F8PS2G0.5	0.176	0.351	0.314	0.438	0.450	0.575	0.476	0.591
F6PS4G0.5	0.169	0.348	0.206	0.472	0.209	0.492	0.209	0.492
F8PS4G0.5	0.173	0.372	0.213	0.498	0.220	0.536	0.220	0.536
F4PS2G1.0	0.210	0.245	0.410	0.225	0.573	0.248	0.609	0.286
F6PS2G1.0	0.187	0.255	0.386	0.252	0.640	0.346	0.704	0.390
F8PS2G1.0	0.177	0.341	0.331	0.395	0.578	0.481	0.668	0.509
F6PS4G1.0	0.186	0.257	0.376	0.259	0.551	0.421	0.588	0.449
F8PS4G1.0	0.178	0.347	0.330	0.397	0.524	0.462	0.549	0.477
F6P4G0.50	0.187	0.266	0.387	0.226	0.691	0.357	0.854	0.401
F8P4G0.50	0.180	0.344	0.343	0.352	0.627	0.452	0.770	0.527
F4P2G1.0	0.210	0.245	0.415	0.228	0.737	0.254	1.027	0.277
F6P2G1.0	0.187	0.255	0.388	0.253	0.704	0.369	0.897	0.432
F8P2G1.0	0.177	0.340	0.331	0.396	0.614	0.471	0.749	0.520
F6P4G1.0	0.186	0.258	0.377	0.258	0.670	0.374	0.824	0.418
F8P4G1.0	0.178	0.347	0.329	0.386	0.649	0.497	0.749	0.518

7. Conclusions

The proposed study presents a comprehensive investigation of the pounding effects for several case studies representing several critical pounding configurations of adjacent non-seismically designed RC structures. The selected structures include configurations that involve different separation distance values and that exhibit floor-to-floor pounding, floor-to-column pounding, pounding between structures with a significant height difference, and pounding between buildings with a significant mass difference. The behaviour of these pounding configurations was analysed for fifty ground motion records using IDA and compared with that of the corresponding control cases (i.e., individual structures with no interaction with other structures). The results provided detailed insights about the type of failure mechanism that contributes to the global collapse of the different configurations and about the influence of the separation distance value. Fragility functions were also developed for different limit states based on these results in order to extract further conclusions regarding the overall influence of certain characteristics of the selected configurations.

Based on the results that were obtained, it can generally be concluded that configurations involving floor-to-column pounding of adjacent buildings are much more likely to exhibit a fragile behaviour due to the large number of cases where global collapse was governed by shear failure. This type of collapse was also found to be more frequent in configurations with structures that have a closer number of storeys. On the contrary, configurations involving floor-to-floor pounding exhibit a better performance. Even though this performance is still worse than that of the corresponding control cases, particularly for higher IM values, the global collapse of the worst performing cases involving floor-to-floor pounding is still mostly governed by ductile mechanisms (flexural failure or flexural-shear failure). In addition, contrary to what is seen for configurations with floor-to-column pounding, the performance of the structures with floor-to-floor pounding is worse when the difference in the number of storeys of the structures involved is larger.

The results that were obtained also indicate that, when floor-to-floor pounding is involved, the likelihood of having a critical storey (a storey that governs the global failure mechanism) above the pounding level increases, particularly when the stiffness of the adjacent structure is larger. Furthermore, the results also show that a larger difference between the heights of adjacent buildings increases the chance of failure of the taller building at a level above the height of the shorter building. When floor-to-column pounding is involved, the critical storey is likely to be that of the pounding level. Regarding the effect of the separation distance, when floor-to-floor pounding is involved, the performance of the structures is generally seen to be very similar, irrespective of the value that is considered for the separation distance. On the contrary, for configurations involving floor-to-column pounding, the value of the separation distance has a large impact on the global behaviour, particularly for higher limit states where the occurrence of global collapse governed by shear failure is inevitable. In these cases, larger values of the separation distance are able to delay the occurrence of brittle failure (i.e., it will occur for larger IM values) and lead to a better structural performance.

Finally, the results of the current study indicate that large scale seismic risk assessment studies should consider fragility functions accounting for different pounding configurations when dealing with building portfolios for which the possibility of pounding is not negligible. Still, for buildings likely to undergo floor-to-floor pounding, the results of the current study indicate that the fragility functions developed for buildings without considering pounding can be used since they are not likely to lead to significant errors. Nevertheless, further research studies similar to the one presented herein should be carried out to analyse the behaviour of other adjacent building configurations and consider the influence of other parameters, such as the presence of infill walls, given their impact on the global performance of RC structures [103–110], in order to generalise these conclusions.

Supplementary Materials: The following are available online at https://www.mdpi.com/article/10.3390/buildings11120665/s1, Figure S1: IDA curves obtained for all considered pounding configura-

tions, Table S1: Characteristics of the selected ground motions.

Author Contributions: Conceptualization, H.M. and X.R.; Formal analysis, H.M. and X.R.; Methodology, H.M. and X.R.; Writing—original draft, H.M. and X.R.; Writing—review & editing, H.M. and X.R. All authors have read and agreed to the published version of the manuscript.

Funding: This research was supported by the grant UIDB/04708/2020 of CONSTRUCT—Instituto de I&D em Estruturas e Construções, funded by national funds through FCT/MCTES (PIDDAC).

Institutional Review Board Statement: Not applicable.

Informed Consent Statement: Not applicable.

Data Availability Statement: The data presented in this study are available on request from the corresponding author.

Conflicts of Interest: The authors declare no conflict of interest.

References

1. Silva, V.; Crowley, H.; Varum, H.; Pinho, R. Seismic risk assessment for mainland Portugal. *Bull. Earthq. Eng.* **2015**, *13*, 429–457. [CrossRef]
2. Martins, L.; Silva, V. Development of a fragility and vulnerability model for global seismic risk analyses. *Bull. Earthq. Eng.* **2021**, *19*, 6719–6745. [CrossRef]
3. D'Ayala, D.; Meslem, A.; Vamvatsikos, D.; Porter, K.; Rossetto, T.; Crowley, H.; Silva, V. *Guidelines for Analytical Vulnerability Assessment of Low/Mid-Rise Buildings—Methodology*; Vulnerability Global Component Project; GEM Technical Report; GEM: Pavia, Italy, 2014.
4. Martins, L.; Silva, V.; Crowley, H.; Cavalieri, F. Vulnerability modellers toolkit, an open-source platform for vulnerability analysis. *Bull. Earthq. Eng.* **2021**, *19*, 5691–5709. [CrossRef]
5. Silva, A.; Macedo, L.; Monteiro, R.; Castro, J.M. Earthquake-induced loss assessment of steel buildings designed to Eurocode 8. *Eng. Struct.* **2020**, *208*, 110244. [CrossRef]
6. Villar-Vega, M.; Silva, V.; Crowley, H.; Yepes, C.; Tarque, N.; Acevedo, A.B.; Hube, M.A.; Gustavo, C.D.; María, H.S. Development of a fragility model for the residential building stock in South America. *Earthq. Spectra* **2017**, *33*, 581–604. [CrossRef]
7. Silva, V.; Crowley, H.; Varum, H.; Pinho, R.; Sousa, L. Investigation of the characteristics of Portuguese regular moment-frame RC buildings and development of a vulnerability model. *Bull. Earthq. Eng.* **2015**, *13*, 1455–1490. [CrossRef]
8. Chouw, N.; Hao, H. Pounding damage to buildings and bridges in the 22 February 2011 Christchurch earthquake. *Int. J. Prot. Struct.* **2012**, *3*, 123–139. [CrossRef]
9. Cole, G.L.; Dhakal, R.P.; Turner, F.M. Building pounding damage observed in the 2011 Christchurch earthquake. *Earthq. Eng. Struct. Dyn.* **2012**, *41*, 893–913. [CrossRef]
10. Favvata, M.; Karayannis, C.; Anagnostopoulou, V. Influence of infill panels with and without openings on the pounding effect of RC structures. In Proceedings of the 15th World Conference on Earthquake Engineering, Lisbon, Portugal, 24–28 September 2012.
11. Khatiwada, S.; Chouw, N. A shake table investigation on interaction between buildings in a row. *Coupled Syst. Mech. Int. J.* **2013**, *2*, 175–190. [CrossRef]
12. Castañeda, Á.E.; Bravo, Y.M. Overview of the structural behavior of columns, beams, floor slabs and buildings during the earthquake of 2016 in Ecuador. *Revista Ingeniería de Construcción* **2018**, *32*, 157–172. [CrossRef]
13. Shrestha, B.; Hao, H. Building pounding damages observed during the 2015 Gorkha earthquake. *J. Perform. Constr. Facilities.* **2018**, *32*, 04018006. [CrossRef]
14. Doğan, M.; Günaydin, A. Pounding of adjacent RC buildings during seismic loads. *Eskişehir Osmangazi Üniversitesi Mühendislik ve Mimarlık Fakültesi Dergisi* **2009**, *22*, 129–145.
15. Jeng, V.; Tzeng, W.L. Assessment of seismic pounding hazard for Taipei City. *Eng. Struct.* **2000**, *22*, 459–471. [CrossRef]
16. ASCE/SEI-7-16. *Minimum Design Loads and Associated Criteria for Buildings and Other Structures*; American Society of Civil Engineers: Reston, VA, USA, 2017.
17. EN1998-1. *Eurocode 8: Design of Structures for Earthquake Resistance—Part 1: General Rules, Seismic Actions and Rules for Buildings*; European Committee for Standardization: Brussels, Belgium, 2005.
18. EC201. *Egyptian Code for Calculating Loads and Forces in Structural Work and Masonry (Code N 201–Ministerial Decision 431/2011)*; Housing and Building National Research Center (HBRC), Ministry of Housing, Utilities and Urban Planning: Giza, Egypt, 2012. (In Arabic)
19. Kazemi, F.; Miari, M.; Jankowski, R. Investigating the effects of structural pounding on the seismic performance of adjacent RC and steel MRFs. *Bull. Earthq. Eng.* **2021**, *19*, 317–343. [CrossRef]
20. Terenzi, G.; Fuso, E.; Sorace, S.; Costoli, I. Enhanced seismic retrofit of a reinforced concrete building of architectural interest. *Buildings* **2020**, *10*, 211. [CrossRef]
21. Cole, G.; Dhakal, R.; Carr, A.; Bull, D. *Building Pounding State of the Art: Identifying Structures Vulnerable to Pounding Damage*; NZSEE Conference; New Zealand Society for Earthquake Engineering Inc.: Wellington, New Zealand, 2010.

22. Kazemi, F.; Mohebi, B.; Jankowski, R. Predicting the seismic collapse capacity of adjacent SMRFs retrofitted with fluid viscous dampers in pounding condition. *Mech. Syst. Signal Process.* **2021**, *161*, 107939. [CrossRef]
23. Kazemi, F.; Mohebi, B.; Yakhchalian, M. Evaluation the P-delta effect on collapse capacity of adjacent structures subjected to far-field ground motions. *Civ. Eng. J.* **2018**, *4*, 1066. [CrossRef]
24. Karayannis, C.G.; Favvata, M.J. Earthquake-induced interaction between adjacent reinforced concrete structures with non-equal heights. *Earthq. Eng. Struct. Dyn.* **2005**, *34*, 1–20. [CrossRef]
25. Jankowski, R. Experimental study on earthquake-induced pounding between structural elements made of different building materials. *Earthq. Eng. Struct. Dyn.* **2009**, *39*, 343–354. [CrossRef]
26. Skrekas, P.; Sextos, A.; Giaralis, A. Influence of bi-directional seismic pounding on the inelastic demand distribution of three adjacent multi-storey R/C buildings. *Earthq. Struct.* **2014**, *6*, 71–87. [CrossRef]
27. Polycarpou, P.C.; Papaloizou, L.; Komodromos, P. An efficient methodology for simulating earthquake-induced 3D pounding of buildings. *Earthq. Eng. Struct. Dyn.* **2014**, *43*, 985–1003. [CrossRef]
28. Bertero, V.V.; Collins, R.G. *Investigation of the Failures of the Olive View Stairtowers during the San Fernando Earthquake and Their Implications on Seismic Design*; Earthquake Engineering Research Center, University of California: Berkeley, CA, USA, 1973.
29. Berg, G.; Degenkolb, H. *Engineering Lessons from the Managua Earthquake*; American Iron and Steel Institute: Washington, DC, USA, 1973.
30. Khatami, S.M.; Naderpour, H.; Barros, R.C.; Jakubczyk-Gałczyńska, A.; Jankowski, R. Determination of peak impact force for buildings exposed to structural pounding during earthquakes. *Geosciences* **2020**, *10*, 18. [CrossRef]
31. Bamer, F.; Strubel, N.; Shi, J.; Markert, B. A visco-elastoplastic pounding damage formulation. *Eng. Struct.* **2019**, *197*, 109373. [CrossRef]
32. Abdel Raheem, S.E.; Fooly, M.Y.M.; Abdel Shafy, A.G.A.; Taha, A.M.; Abbas, Y.A.; Abdel Latif, M.M.S. Numerical simulation of potential seismic pounding among adjacent buildings in series. *Bull. Earthq. Eng.* **2019**, *17*, 439–471. [CrossRef]
33. Elwardany, H.; Seleemah, A.; Jankowski, R.; El-khoriby, S. Influence of soil–structure interaction on seismic pounding between steel frame buildings considering the effect of infill panels. *Bull. Earthq. Eng.* **2019**, *17*, 6165–6202. [CrossRef]
34. Kharazian, A.; López-Almansa, F. State-of-the-art of research on seismic pounding between buildings with aligned slabs. *Arch. Comput. Methods Eng.* **2019**, *26*, 327–345. [CrossRef]
35. Naeej, M.; Vaseghi Amiri, J.; Jalali, S.G. Stochastic analysis of adjacent structures subjected to structural pounding under earthquake excitation. *J. Rehabil. Civ. Eng.* **2019**, *7*, 153–165.
36. Yang, Y.; Li, S. Development of a refined analysis method for earthquake-induced pounding between adjacent RC frame structures. *Sustainability* **2019**, *11*, 4928. [CrossRef]
37. Hao, H. Analysis of seismic pounding between adjacent buildings. *Aust. J. Struct. Eng.* **2015**, *16*, 208–225. [CrossRef]
38. Jankowski, R.; Seleemah, A.; El-Khoriby, S.; Elwardany, H. Experimental study on pounding between structures during damaging earthquakes. In *Key Engineering Materials*; Trans Tech Publications: Bäch, Switzerland, 2015; pp. 249–252.
39. Cui, L.L.; Guo, A.X.; Li, H. Investigation of the parameters of Hertz impact model for the pounding analysis of highway bridge. *Procedia Eng.* **2011**, *14*, 2773–2778. [CrossRef]
40. Rezavandi, A.; Moghadam, A.S. Experimental and numerical study on pounding effects and mitigation techniques for adjacent structures. *Adv. Struct. Eng.* **2007**, *10*, 121–134. [CrossRef]
41. Filiatrault, A.; Wagner, P.; Cherry, S. An experimental study on the seismic pounding of buildings. In Proceedings of the Eleventh World Conference on Earthquake Engineering, Acapulco, Mexico, 23–28 June 1996.
42. Filiatrault, A.; Wagner, P.; Cherry, S. Analytical prediction of experimental building pounding. *Earthq. Eng. Struct. Dyn.* **1995**, *24*, 1131–1154. [CrossRef]
43. Jankowski, R. State-of-the-art of research on seismic pounding between buildings with aligned slabs; Letter to the editor: Discussion on the paper. *Arch. Comput. Methods Eng.* **2019**, *26*, 531–532. [CrossRef]
44. Jankowski, R. Non-linear viscoelastic modelling of earthquake-induced structural pounding. *Earthq. Eng. Struct. Dyn.* **2005**, *34*, 595–611. [CrossRef]
45. Jankowski, R.; Wilde, K.; Fujino, Y. Pounding of superstructure segments in isolated elevated bridge during earthquakes. *Earthq. Eng. Struct. Dyn.* **1998**, *27*, 487–502. [CrossRef]
46. Favvata, M.J.; Karayannis, C.G. The inter-storey pounding effect on the seismic behaviour of infilled and pilotis RC structures. In *Seismic Behaviour and Design of Irregular and Complex Civil Structures*; Lavan, O., De Stefano, M., Eds.; Springer Netherlands: Dordrecht, The Netherlands, 2013; pp. 87–101.
47. Flenga, M.G.; Favvata, M.J. Probabilistic seismic assessment of the pounding risk based on the local demands of a multistory RC frame structure. *Eng. Struct.* **2021**, *245*, 112789. [CrossRef]
48. Flenga, M.G.; Favvata, M.J. Fragility curves and probabilistic seismic demand models on the seismic assessment of RC frames subjected to structural pounding. *Appl. Sci.* **2021**, *11*, 8253. [CrossRef]
49. Vamvatsikos, D.; Cornell, C.A. Incremental dynamic analysis. *Earthq. Eng. Struct. Dyn.* **2002**, *31*, 491–514. [CrossRef]
50. El-Kholy, A.M.; Sayed, H.; Shaheen, A.A. Comparison of Egyptian code 2012 with Eurocode 8-2013, IBC 2015 and UBC 1997 for seismic analysis of residential shear-walls RC buildings in Egypt. *Ain Shams Eng. J.* **2018**, *9*, 3425–3436. [CrossRef]
51. McKenna, F. OpenSees: A framework for earthquake engineering simulation. *Comput. Sci. Eng.* **2011**, *13*, 58–66. [CrossRef]

52. Ibarra, L.F.; Krawinkler, H. *Global Collapse of Frame Structures Under Seismic Excitations*; Pacific Earthquake Engineering Research Center: Berkeley, CA, USA, 2005.
53. Lignos, D.G.; Krawinkler, H. Deterioration modeling of steel components in support of collapse prediction of steel moment frames under earthquake loading. *J. Struct. Eng.* **2011**, *137*, 1291–1302. [CrossRef]
54. Haselton, C.B.; Liel, A.B.; Taylor-Lange, S.C.; Deierlein, G.G. Calibration of model to simulate response of reinforced concrete beam-columns to collapse. *ACI Struct. J.* **2016**, *113*, 1141–1152. [CrossRef]
55. Jeon, J.-S.; Lowes, L.N.; DesRoches, R.; Brilakis, I. Fragility curves for non-ductile reinforced concrete frames that exhibit different component response mechanisms. *Eng. Struct.* **2015**, *85*, 127–143. [CrossRef]
56. Elwood, K.J. Modelling failures in existing reinforced concrete columns. *Can. J. Civ. Eng.* **2004**, *31*, 846–859. [CrossRef]
57. Baradaran, S.M.; Elwood, K.J. Mechanical model for non ductile reinforced concrete columns. *J. Earthq. Eng.* **2013**, *17*, 937–957. [CrossRef]
58. Panagiotakos, T.B.; Fardis, M.N. Deformations of reinforced concrete members at yielding and ultimate. *Struct. J.* **2001**, *98*, 135–148.
59. Elwood, K.J.; Moehle, J.P. *Shake Table Tests and Analytical Studies on the Gravity Load Collapse of Reinforced Concrete Frames, PEER Report 2003/01*; Pacific Earthquake Engineering Research Center, College of Engineering, University of California: Berkeley, CA, USA, 2003.
60. Sezen, H.; Moehle Jack, P. Shear strength model for lightly reinforced concrete columns. *J. Struct. Eng.* **2004**, *130*, 1692–1703. [CrossRef]
61. ASCE. *Seismic Evaluation and Retrofit of Existing Buildings (ASCE/SEI 41-17)*; American Society of Civil Engineers: Reston, VA, USA, 2017.
62. Park, R.; Paulay, T. *Reinforced Concrete Structures*; John Wiley & Sons: Hoboken, NJ, USA, 1975.
63. Skoulidou, D.; Romão, X.; Franchin, P. How is collapse risk of RC buildings affected by the angle of seismic incidence? *Earthq. Eng. Struct. Dyn.* **2019**, *48*, 1575–1594. [CrossRef]
64. Dolšek, M.; Fajfar, P. *Post-Test Analyses of the SPEAR Test Building*; University of Ljubljana: Ljubljana, Slovenia, 2005.
65. DesRoches, R.; Muthukumar, S. Effect of pounding and restrainers on seismic response of multiple-frame bridges. *J. Struct. Eng.* **2002**, *128*, 860–869. [CrossRef]
66. Goldsmith, W. *Impact: The Theory and Physical Behaviour of Colliding Solids*; Edward Arnold: London, UK, 1961.
67. Ruangrassamee, A.; Kawashima, K. Relative displacement response spectra with pounding effect. *Earthq. Eng. Struct. Dyn.* **2001**, *30*, 1511–1538. [CrossRef]
68. Maison Bruce, F.; Kasai, K. Analysis for a type of structural pounding. *J. Struct. Eng.* **1990**, *116*, 957–977. [CrossRef]
69. Maison, B.F.; Kasai, K. Dynamics of pounding when two buildings collide. *Earthq. Eng. Struct. Dyn.* **1992**, *21*, 771–786. [CrossRef]
70. Muthukumar, S.; DesRoches, R. A Hertz contact model with non-linear damping for pounding simulation. *Earthq. Eng. Struct. Dyn.* **2006**, *35*, 811–828. [CrossRef]
71. Anagnostopoulos, S.A. Pounding of buildings in series during earthquakes. *Earthq. Eng. Struct. Dyn.* **1988**, *16*, 443–456. [CrossRef]
72. Abdel Raheem, S.E. Pounding mitigation and unseating prevention at expansion joints of isolated multi-span bridges. *Eng. Struct.* **2009**, *31*, 2345–2356. [CrossRef]
73. Karayannis, C.G.; Naoum, M.C. Torsional behavior of multistory RC frame structures due to asymmetric seismic interaction. *Eng. Struct.* **2018**, *163*, 93–111. [CrossRef]
74. Anagnostopoulos, S.A. Equivalent viscous damping for modeling inelastic impacts in earthquake pounding problems. *Earthq. Eng. Struct. Dyn.* **2004**, *33*, 897–902. [CrossRef]
75. Mahmoud, S.; Jankowski, R. Elastic and inelastic multi-storey buildings under earthquake excitation with the effect of pounding. *J. Appl. Sci.* **2009**, *9*, 3250–3262. [CrossRef]
76. Mahmoud, S.; Jankowski, R. Modified linear viscoelastic model of earthquake-induced structural pounding. *Trans. Civ. Environ. Eng.* **2011**, *35*, 51–62.
77. Polycarpou, P.C.; Komodromos, P. Earthquake-induced poundings of a seismically isolated building with adjacent structures. *Eng. Struct.* **2010**, *32*, 1937–1951. [CrossRef]
78. Azevedo, J.; Bento, R. Design criteria for buildings subjected to pounding. In Proceedings of the Eleventh World Conference on Earthquake Engineering, Acapulco, Mexico, 23–28 June 1996.
79. Khatiwada, S.; Larkin, T.; Chouw, N. Influence of mass and contact surface on pounding response of RC structures. *Earthq. Struct.* **2014**, *7*, 385–400. [CrossRef]
80. Kohrangi, M.; Bazzurro, P.; Vamvatsikos, D. Vector and scalar IMs in structural response estimation, part II: Building demand assessment. *Earthq. Spectra* **2016**, *32*, 1525–1543. [CrossRef]
81. Gentile, R.; Galasso, C. Accounting for directivity-induced pulse-like ground motions in building portfolio loss assessment. *Bull. Earthq. Eng.* **2020**, *19*, 6303–6328. [CrossRef]
82. Kohrangi, M.; Kotha, S.R.; Bazzurro, P. Ground-motion models for average spectral acceleration in a period range: Direct and indirect methods. *Bull. Earthq. Eng.* **2018**, *16*, 45–65. [CrossRef]
83. Ancheta, T.D.; Darragh, R.B.; Stewart, J.P.; Seyhan, E.; Silva, W.J.; Chiou, B.S.J.; Wooddell, K.E.; Graves, R.W.; Kottke, A.R.; Boore, D.M.; et al. NGA-West2 database. *Earthq. Spectra* **2014**, *30*, 989–1005. [CrossRef]

84. Macedo, L.; Castro, J.M. SelEQ: An advanced ground motion record selection and scaling framework. *Adv. Eng. Softw.* **2017**, *114*, 32–47. [CrossRef]
85. Ricci, P.; De Risi, M.T.; Verderame, G.M.; Manfredi, G. Procedures for calibration of linear models for damage limitation in design of masonry-infilled RC frames. *Earthq. Eng. Struct. Dyn.* **2016**, *45*, 1315–1335. [CrossRef]
86. Rossetto, T.; Elnashai, A. Derivation of vulnerability functions for European-type RC structures based on observational data. *Eng. Struct.* **2003**, *25*, 1241–1263. [CrossRef]
87. Rossetto, T.; Elnashai, A. A new analytical procedure for the derivation of displacement-based vulnerability curves for populations of RC structures. *Eng. Struct.* **2005**, *27*, 397–409. [CrossRef]
88. Ghobarah, A. On drift limits with different damage levels. In Proceedings of the International Workshop on Performance-Based Seismic Design Concepts and Implementation, Bled, Slovenia, 28 June–1 July 2004.
89. Federal Emergency Management Agency. *Prestandard and Commentary for Seismic Rehabilitation of Buildings*; FEMA-356; Federal Emergency Management Agency: Washington, DC, USA, 2000.
90. Federal Emergency Management Agency. *NEHRP Guidelines for the Seismic Rehabilitation of Buildings*; FEMA-273; Federal Emergency Management Agency: Washington, DC, USA, 1997.
91. NBCC. *National Building Code of Canada. Ottawa*; National Research Council: Ottawa, ON, Canada, 2010.
92. IBC. *International Building Code*; International Code Council: Washington, DC, USA, 2009.
93. *Structural Design Actions-Part 4: Earthquake Actions in Australia AS1170-4 A*; Committee BD-006, General Design Requirements and Loading on Structures, Council of Standards Australia: Sydney, Australia, 2007.
94. Krawinkler, H.; Seneviratna, G.D.P.K. Pros and cons of a pushover analysis of seismic performance evaluation. *Eng. Struct.* **1998**, *20*, 452–464. [CrossRef]
95. Crowley, H.; Despotaki, V.; Silva, V.; Dabbeek, J.; Romão, X.; Pereira, N.; Castro, J.M.; Daniell, J.; Veliu, E.; Bilgin, H.; et al. Model of seismic design lateral force levels for the existing reinforced concrete European building stock. *Bull. Earthq. Eng.* **2021**, *19*, 2839–2865. [CrossRef]
96. Romão, X.; Delgado, R.; Costa, A. Assessment of the statistical distributions of structural demand under earthquake loading. *J. Earthq. Eng.* **2011**, *15*, 724–753. [CrossRef]
97. Mohamed, H. Seismic Risk Assessment of Reinforced Concrete Frames with Masonry Infill. Ph.D. Thesis, University of Porto, Porto, Portugal, 2017.
98. Shapiro, S.S.; Wilk, M.B. An analysis of variance test for normality (complete samples). *Biometrika* **1965**, *52*, 591–611. [CrossRef]
99. Romão, X.; Delgado, R.; Costa, A. An empirical power comparison of univariate goodness-of-fit tests for normality. *J. Stat. Comput. Simul.* **2010**, *80*, 545–591. [CrossRef]
100. Skoulidou, D.; Romão, X. Uncertainty quantification of fragility and risk estimates due to seismic input variability and capacity model uncertainty. *Eng. Struct.* **2019**, *195*, 425–437. [CrossRef]
101. Romão, X.; Delgado, R.; Costa, A. Statistical characterization of structural demand under earthquake loading. Part 1: Robust estimation of the central value of the data. *J. Earthq. Eng.* **2012**, *16*, 686–718. [CrossRef]
102. Romão, X.; Delgado, R.; Costa, A. Statistical characterization of structural demand under earthquake loading. Part 2: Robust estimation of the dispersion of the data. *J. Earthq. Eng.* **2012**, *16*, 864–896. [CrossRef]
103. Asteris, G.P. Modeling of infilled frames with openings. *Open Constr. Build. Technol. J.* **2012**, *6*, 81–91. [CrossRef]
104. Mohamed, H.; Romão, X. Analysis of the performance of strut models to simulate the seismic behaviour of masonry infills in partially infilled RC frames. *Eng. Struct.* **2020**, *222*, 111124. [CrossRef]
105. Mohamed, H.; Romão, X. Robust calibration of macro-models for the in-plane behavior of masonry infilled RC frames. *J. Earthq. Eng.* **2018**, *25*, 407–433. [CrossRef]
106. Mohamed, H.; Romão, X. Performance analysis of a detailed FE modelling strategy to simulate the behaviour of masonry-infilled RC frames under cyclic loading. *Earthq. Struct.* **2018**, *14*, 551–565.
107. Asteris, G.P.; Cotsovos, D.M. Numerical investigation of the effect of infill walls on the structural response of RC frames. *Open Constr. Build. Technol. J.* **2012**, *6*, 164–181. [CrossRef]
108. Sattar, S.; Liel, A.B. Seismic performance of reinforced concrete frame structures with and without masonry infill walls. In Proceedings of the 9th US National and 10th Canadian Conference on Earthquake Engineering, Toronto, ON, Canada, 25–29 July 2010.
109. Sattar, S.; Liel, A.B. Seismic performance of nonductile reinforced concrete frames with masonry infill walls: II. Collapse assessment. *Earthq. Spectra* **2016**, *32*, 819–842. [CrossRef]
110. Sattar, S.; Liel, A.B. Seismic performance of nonductile reinforced concrete frames with masonry infill walls: I. Development of a strut model enhanced by finite element models. *Earthq. Spectra* **2016**, *32*, 795–818. [CrossRef]